Technische Universität Ilmenau

Fakultät Informatik und Automatisierung
Fachgebiet Regelungstechnik

Bachelor Thesis

Contact Detection of the SCOUT Rimless-Wheels Through Motor Current Analysis

submitted by

Justus Jentsch

Matrikelnummer:	61666
Studiengang:	Technische Kybernetik und Systemtheorie
verantw. Hochschullehrer:	Prof. Dr.-Ing. Johann Reger
wissenschaftlicher Betreuer:	M.Sc. Manuel Schütt
eingereicht am:	March 26, 2024

Eigenständigkeitserklärung

Die vorliegende Arbeit habe ich selbstständig ohne Benutzung anderer als der angegebenen Quellen angefertigt. Alle Stellen, die wörtlich oder sinngemäß aus veröffentlichten Quellen entnommen wurden, sind als solche kenntlich gemacht. Die Arbeit ist in gleicher oder ähnlicher Form oder auszugsweise im Rahmen einer oder anderer Prüfungen noch nicht vorgelegt worden.

Ilmenau, March 26, 2024 Justus Jentsch

Acknowledgements

I would like to express my sincere gratitude to my supervisor from the TU Ilmenau, Prof. Dr. Johann Reger, for his invaluable guidance and mentorship throughout the course of my thesis. His expertise and encouragement have been instrumental in shaping the direction and quality of this work.

I extend my thanks to Manuel Schütt, my supervisor at the German Aerospace Centre (DLR), for his insightful inputs, constructive feedback, and continuous encouragement. His expertise in the field has significantly contributed to the development and success of this thesis.

Special appreciation goes to my colleagues at DLR. Antoine Pignede for his expertise on Dymola Simulations and Dario Lizio and Johannes Koch for their valuable contributions to experiments throughout my thesis. Their collaborative spirit and specialised knowledge have enriched the overall quality of this research.

I am grateful to the German Aerospace Centre (DLR) for providing me with the opportunity to undertake this research project. The resources, support, and conducive research environment at DLR have played a central role in the successful outcome of this thesis.

Lastly, I would like to express my deepest thanks to my family, friends, and my girlfriend Emelie for their unwavering support and encouragement throughout this thesis and my academic journey. Their understanding, patience, and belief in my abilities have been my pillars of strength.

Abstract

The SCOUT-Rover is being developed at the German Aerospace Centre (DLR) and is designed for terrestrial and extraterrestrial missions. These missions range from rescue operations in challenging environments to the exploration of astronomical objects such as Mars and Earth's Moon. A key aspect lies in efficient locomotion, especially with the unique Rimless-Wheels, which are designed for navigating through rough terrain. Effective detection of ground contacts is crucial for improving ride quality. This study includes mathematical modelling and simulation of the rover's locomotion system as well as dimensional data acquisition tests. An onboard contact detection program was developed to evaluate the motor currents and estimate contacts based on the model created. These methods were successfully validated for a future rover prototype. The onboard contact detection program for the SCOUT-Rover has promising effects on its operational performance and lifetime and has potential applications in terrestrial and extraterrestrial environments.

Kurzfassung

Der SCOUT-Rover wird am Deutschen Zentrum für Luft- und Raumfahrt (DLR) entwickelt und ist für terrestrische und extraterrestrische Missionen konzipiert. Diese Missionen reichen von Rettungseinsätzen in anspruchsvollen Umgebungen bis hin zur Erforschung von Himmelskörpern wie dem Mars und dem Mond. Ein entscheidender Aspekt liegt in effizienter Fortbewegung, insbesondere Lokomotion durch herausforderndes Gelände unerlässlich sind. Eine effektive Erkennung des Bodenkontakts ist entscheidend für die Verbesserung der Fahrqualität. Die Arbeit umfasst die mathematische Modellierung und Simulation des Antriebssystems des Rovers sowie Tests zur Erfassung von Dimensionaldaten. Ein Onboard-Kontakterkennungsprogramm wurde für die Auswertung der Motorströme entwickelt, das auf Basis des erstellten Modells eine Kontaktschätzung vornimmt. Diese Methoden wurden erfolgreich validiert für einen bevorstehenden Rover-Prototypen. Das Onboard-Kontakterkennungsprogramm im SCOUT-Rover hat vielversprechende Auswirkungen auf seine Betriebsleistung, Lebensdauer und potenzielle Anwendungen in terrestrischen und extraterrestrischen Umgebungen.

Contents

List of Abbreviations

CAD	Computer-Aided Design
FPS	Frames per Second
HDF5	Hierarchical Data Format (5)
IMU	Inertial Measurement Unit
LED	Light Emitting Diode
MMX	Martian Moon eXploration
OBC	OnBoard Computer
PDMS	Polydimethylsiloxane
POM	Polyoxymethylene
TPU	Thermoplastic Polyurethane
ROLV	Rolling Leg Vehicle
ROS2	Robot Operating System (2)
rpm	Rotations per Minute
SCOUT	Space Cave explOration UniT
Wheg	Legged Wheel

List of Symbols

θ	Coordinate origin for wheel rotation
$\varphi(t)$	Time-dependent rotation angle
$\varphi_{\mathrm{M}}(t)$	Motor angle
$\varphi_{\mathrm{W}}(t)$	Wheel angle
$\omega(t)$	Angular velocity
$\omega_{\mathrm{M}}(t)$	Motor angular velocity
$\omega_{\mathrm{W}}(t)$	Wheel angular velocity
$\alpha(t)$	Time-dependent angular acceleration
$\alpha_{\mathrm{M}}(t)$	Motor angular acceleration
$\alpha_{\mathrm{W}}(t)$	Wheel angular acceleration
Z	Identifier for cylinder
b_c	Wheel width
s_H	Side length of hexagon
r	Radius
$\mathbf{r}_\perp$	Radial vector orthogonal to rotation axis
r_c	Radius of cylinder
r_i	Inner radius of hollow cylinder
r_o	Outer radius of hollow cylinder
l_S	Length of spoke
h_F	Height of foot
d	Diameter
d_H	Inner diameter of hexagon
A	Area
A_H	Area of hexagon
A_c	Area of cylinder
V_c	Volume of cylinder

m	Mass
m_M	Mass of wheel mounting
m_S	Mass of spoke
m_F	Mass of foot
m_{SCT}	Mass of the SCOUT-Rover
Q	Weight scaling factor for individual motor load
ρ	Density
J	Inertia of masses
J_Z	Hollow cylinder's interia of masses
J_{tot}	Total inertia of masses
J_{GB}	Gearbox inertia of masses
J_{W}	Wheel's inertia of masses
M	Torque
M_{W}	Wheel torque
M_{GB}	Gearbox torque
M_{R}	Friction torque
M_{M}	Motor torque
M_{des_f}	Desired free wheel torque
M_{des_c}	Desired contact torque
M_{tot}	Total component torque
n_S	Number of spokes in a Rimless-Wheel
υ	Spoke separation angle
ι	Gearbox transmission factor
η	Energy conversion efficiency
η_{GB}	Efficiency of gearbox
η_{M}	Efficiency of motor
$\boldsymbol{\vartheta}$	Contact-point vector
$\boldsymbol{\vartheta}_l$	Constant wheel diameter vector
$\boldsymbol{\vartheta}_r$	Foot radius vector
$c(\varphi)$	Contact distance
E	Energy
E_{R}	Friction energy
W	Work
W_a	Acceleration work
I	Current
I_{M}	Motor current

I_{M_f}	Free wheel motor current
I_{M_c}	Contact motor current
I_{M_r}	Measured (real) motor current
V	Voltage / electrical potential difference
$V_{\mathbf{B}}$	Battery voltage
R	Resistance
R_{M}	Motor resistance
$R_{\mathrm{R}}(t)$	Time-variable potentiometer resistance
P	Power
P_{rot}	Rotational power
P_{el}	Electrical power
P_{rot_f}	Rotational power for free wheel case
P_{el_f}	Electrical power for free wheel case
P_{rot_c}	Rotational power for contact case
P_{el_c}	Electrical power for contact case
F	Force
$\mathbf{F}_g$	Gravitational force
v	Velocity
$\mathbb{A}_f$	Mean value between real and free wheel current
$\mathbb{A}_c$	Mean value between real and contact current
h_t	Time horizon
t_v	Verification time
c_t	Contact threshold
$\mathcal{C}$	$\in \{0, 1\}$ Contact variable
b_u	Upper boundary
b_l	Lower boundary

List of Figures

List of Tables

1. Introduction

This chapter serves to get an idea of the challenges the SCOUT-Rover has to deal with and what this means for detecting contacts. More detailed specifications of the SCOUT-Rover follow an introductory motivation of the rover's mission objectives. These considerations result in a problem definition and the initial question of the thesis. The scientific contribution of the thesis is then outlined, and finally, a brief overview of the following chapters is given.

1.1. Motivation

This research is concerned with the development and the capability extension of the Space Cave explOration UniT (SCOUT) rover platform, created at the German Aerospace Centre (DLR) at the Institute of System Dynamics and Control (SR). Primary mission plans are dedicated to investigate Martian and Lunar caves formed by volcanic activity, requiring a robust and agile rock traversing robot. The SCOUT-Rover's unique design, featuring Rimless-Wheels and a three-segmented structure, enables it to navigate challenging terrains, including drops up to 1.5 meters in rocky areas and caves, without breaking. [LD10]

The significance of exploring lava tubes lies in their potential to support human settlement on Mars. Lava tubes offer natural protection against radiation, a critical factor given Mars' lack of a strong magnetic field and thin atmosphere. Lava tubes could be accessed through openings, so-called Skylights, that can be seen in Figure 1.1. These underground structures also hold promise for providing essential resources and may even harbour microbial life. The research aligns with the broader context of planetary ex-

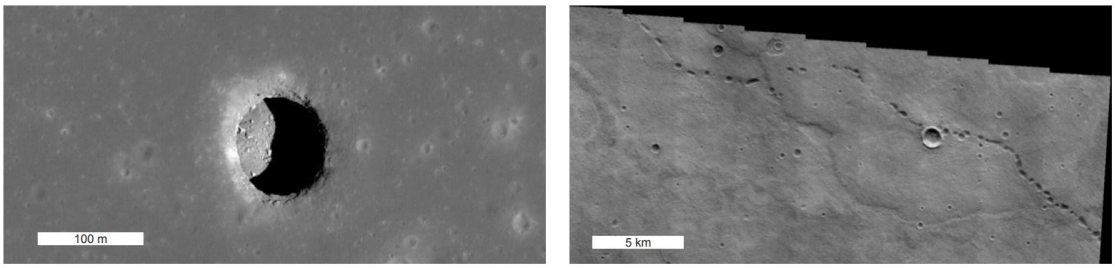

Figure 1.1.: Surface scans of potential Skylights of lava tubes on Earth's Moon (left) and Mars (right). [FBSMa15]

ploration, focusing on Lunar and Martian caves and their potential contributions to the future of space colonisation [FBSMa15].

The SCOUT-Rover is particularly versatile because of its adaptability to terrestrial missions. Beyond extraterrestrial exploration, the rover has applications on Earth, including rescue missions in cave systems and avalanche areas [PSFa23]. The development goals encompass both terrestrial and extraterrestrial applications, reflecting a holistic approach to robotics and space exploration [LSFa23]. In Figure 1.2 the SCOUT-Rover can be seen navigating on Mount Etna, an active volcano on Sicily [PSFa23].

The thesis aims to contribute to the ongoing efforts of the German Aerospace Centre to advance the SCOUT-Rover's functionalities. Specifically, it focuses on implementing contact detection for the specialised Rimless-Wheels, a crucial element for navigating diverse terrains and ensuring the rover's longevity and efficiency.
The research revolves around the question, whether a developed algorithm can recognise contacts based on the motor currents for a Rimless-Wheel on the SCOUT-Rover. To approach this question, mathematical modelling, simulations, and practical tests are carried out to validate the functionality of a possible onboard implementation of the contact detection system.

Figure 1.2.: The SCOUT-Rover in a field test on volcanic regolith on mount Etna. [PSFa23]

1.2. SCOUT-Rover

The SCOUT-Rover is an exceptionally robust and uniquely designed exploration platform specifically developed to navigate challenging environments with Rimless-Wheels. These wheels are subject to extensive testing and a distinctive three-spoked structure. The SCOUT-Rover stands out for its durability and adaptability. [SLBa17a]

In the exploration of cave systems, the SCOUT-Rover operates within solid ground conditions. Unlike other terrestrial self-driving vehicles contending with moving objects, SCOUT benefits from the immovability of its surroundings [LD10]. This static setting facilitates map generation with greater ease, contributing to potentially higher-quality maps. However, the rover's flexible components, while advantageous for traversing rough terrain, introduce a source of erratic movement [LSFa23]. The rover will encounter obstacles like boulders larger than itself, cliffs, crevices and narrow cave entrances. This may impact data quality and localisation accuracy, necessitating halting of the rover [Koc23] or smoothing the ride for measurements, which can be approached with an accurate ground contact detection.

1.3. Problem Definition

In the context of SCOUT's overarching mission to explore extraterrestrial caves, several critical aspects align with the problem at hand. The fact that the rover cannot return to the surface empathises with the need for long operability within the cave environment, so efficient energy consumption is highly important [LSFa23]. Given that motors consume a significant portion of the available energy, enhancing their efficiency emerges as a central challenge.

Efficient motor usage extends beyond bare energy conservation, directly influencing the rover's durability and survivability. Identifying scenarios such as wheels spinning freely in the air or becoming stuck is vital for reducing energy consumption and potential damage to wheels and motors. A robust contact detection system supports achieving these goals.

The strategic decision to minimise the reliance on external sensors aligns with the need for sustainability and durability in harsh environments. Every additional sensor introduces a potential point of failure and increases energy consumption [LSFa23]. Hence, prioritising contact detection using motor currents becomes a promising ambition.
However, this approach comes with its own challenges, as electric motor signals are inherently noisy [Mil15]. Selecting the right filtering mechanisms and developing an effective approach to handle noise emerges as a critical factor for addressing this complex problem.
These considerations level the justification of the general underlying question of this bachelor thesis:

Can a derived algorithm recognise contacts based on the motor currents for a Rimless-Wheel on the SCOUT-Rover?

Balancing the need for accurate current-based contact estimation with the constraints of performance efficiency forms the central objective of this research.

1.4. Thesis Contributions

Initially, the drive chain of the SCOUT-Rover is mathematically modelled, establishing a foundation for subsequent simulations. This enables a comprehensive understanding of the rover's behaviour and is essential for developing the contact detection algorithm.

Building on the mathematical model, the thesis includes a simulation of various scenarios. This step is essential for exploring different cases and understanding the current-behaviour of the rover. The insights gained from the simulation not only inform the development of the contact detection algorithm but also provide valuable information for future projects.

The core contribution centres around the development and implementation of a robust contact detection algorithm for the SCOUT-Rover, a program designed to identify contact of the Rimless-Wheels with the ground.

1.5. Thesis Outline

Chapter 2 offers an overview of the ongoing development of the SCOUT-Rover and sets the stage for the subsequent discussions of the Rimless-Wheel and the current state of Rimless-Wheel driving. Furthermore, approaches for ground contact detection of analogous rovers are discussed.

Chapter 3 provides a comprehensive summary of the general methodologies employed in the modelling of the system. Furthermore, the contact detection logic is explained. Additionally, the case study carried out in Protocol A is explained.

Chapter 4 focuses on the contact detection program and the multi-body simulation model in Dymola. These approaches serve to validate the modelling done in the previous chapter. This chapter further offers a detailed examination of the development of the onboard implementation in ROS2.

The collective outcomes from Chapters 3 and 4 are presented in Chapter 5, where results are discussed and compared.

Chapter 6 approaches a discussion of the overall results, presenting problems and solutions and furthermore extending ideas related to the results. Lastly, an outlook for future research is given.

The last Chapter 7 concludes with a summary of all topics and an answer to the initial question of this thesis.

2. State of the Art

This chapter presents the state of the art in the context of this thesis. First, reference is made to the development status of the SCOUT-Rover. The concept of the Rimless-Wheel is explained, and which rovers currently use these wheel types. Lastly, contact detection concepts are discussed. Sensor technology and the concepts used for contact detection in rovers are discussed in this context.

2.1. SCOUT Platform

Anchored in biologically inspired non-steerable Rimless-Wheels [SLBa17b], SCOUT embraces a modular design to facilitate versatility and adaptability to diverse terrains. The SCOUT-Rover serves as the focal point of this research, constituting a locomotion platform developed by the German Aerospace Centre (DLR) at the Institute of System Dynamics and Control in Oberpfaffenhofen. Utilising a hybrid locomotion mechanism that inherits rolling and walking motions, the rover traverses rough terrain, including steep sand slopes, rocky terrains, and soft soils [PL22].

In Figure 2.1, which is inspired by the works of J. Skibbe, the synchronous wheel configuration on the left hand side and the tripod wheel configuration on the right hand side are depicted. In the publication of Skibbe, different wheel modes for the SCOUT-Rover are discussed and resulting effects on vertical displacement and roll angles are analysed. It also discusses how a controller arranges such phase shifts to enable riding and switching between different wheel modes [Ski21].

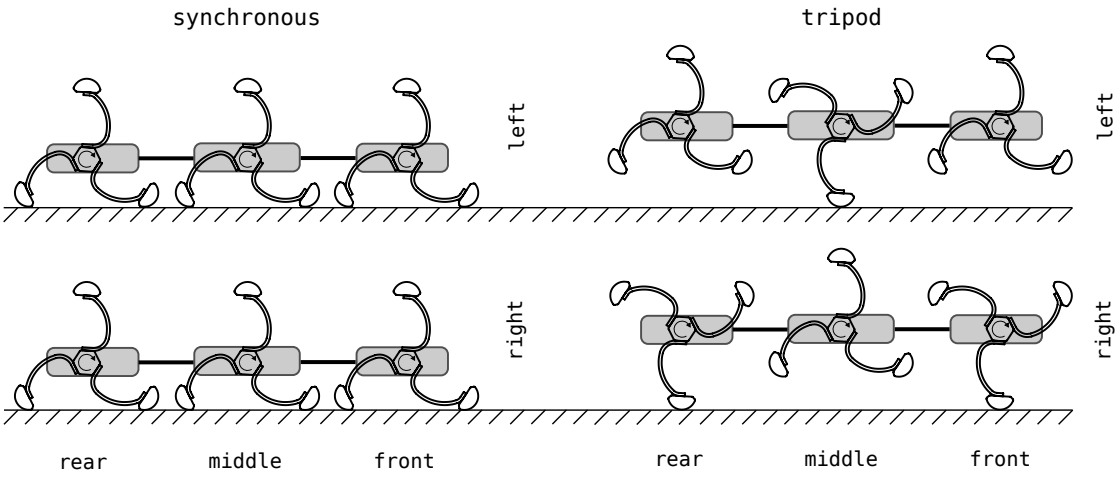

Figure 2.1.: Synchronous and tripod Rimless-Wheel configurations.

2.1.1. Rover Specifications

Key specifications of the SCOUT-Rover are summarised in Table 2.1, providing insights into its dimensions, payload capacity, speed, obstacle traversal capabilities and battery runtime. [LSFa23]

Rover Mass	$\approx$ 18 kg
Payload Capacity	$>$ 12 kg, 10 L volume
Maximum Speed	$\approx$ 1.7 m/s
Max. Obstacle Height	$>$ 400 mm
Tested Drop Height	$>$ 1.5 m
Battery Runtime (Li-Ion)	$\approx$ 10 h
Size of the Rover	1.0 x 0.5 x 0.4 m

Table 2.1.: Specifications of the SCOUT-Rover [LSFa23].

Moreover, the PICO-KBU4 from Aaeon, the development PC driving the SCOUT's operations, features robust specifications, highlighted by a 7th generation Intel® Core™ i5-7300U processor, 16 GB DDR4 memory, and a 512 GB M.2-PCIe-NVMe SSD for storage. [Asu23]

The motor controller can output up to 10 A of current. The controller has an EtherCAT compatibility and communicates at 100 Mbps (Megabytes per Second) with the onboard computer.

The current motor system of the rover is powered by six (RE 40 Ø40 mm) motors from Maxon with Graphite brushes, delivering 150 Watts at 48 V nominal voltage [Max22] each, alongside Planetary Gearheads (GP 42 C 203124), featuring a reduction ratio of 66:1 [Max21b]. A motor is complemented by an Encoder (16 EASY 128–1024 CPT) from Maxon, boasting a supply voltage of 5 V ± 10% and a maximum operating frequency of 1600 kHz [Max21a].

2.1.2. Complete Model of the SCOUT in Dymola

Dymola, which stands for Dynamic Modelling Laboratory is a modelling and simulation tool, based on the Modelica language. Furthermore, Dymola is an influential Modelica tool, which was the first full-scale industrial-strength Modelica environment [FPAa20]. The purpose of this model is to represent physical systems using model libraries that are widely available and used in many engineering domains. The philosophy is to express a system's behaviour not in algorithms but in equations that represent physical laws. It remains with a hierarchical structure that has the most simple of structures at the bottom, such as resistances or springs, and can then be assembled to a system like the SCOUT-Rover.
An extensive library was created that can model the behaviour of the Rimless-Wheels, motors and gearboxes and mainly the SCOUT itself in various scenarios. The SCOUT was fully modelled and simulated in Dymola, with a visual representation made possible by an in-house written visualisation toolbox. Figure 2.2 shows a frame of such a visualisation. [PL22]

2.2. Concept of Rimless-Wheels

To understand the intricacies of contact detection, it is important to explore Rimless-Wheel concepts despite their deviation from traditional tire-and-rim designs. In space exploration scenarios, where traditional gas-filled tyres are impractical, alternative concepts have emerged to facilitate locomotion on extraterrestrial surfaces. While rimmed wheels are suitable for many scenarios, they face limitations in specific environments, necessitating exploring alternative locomotion solutions. Legged concepts, depicted in

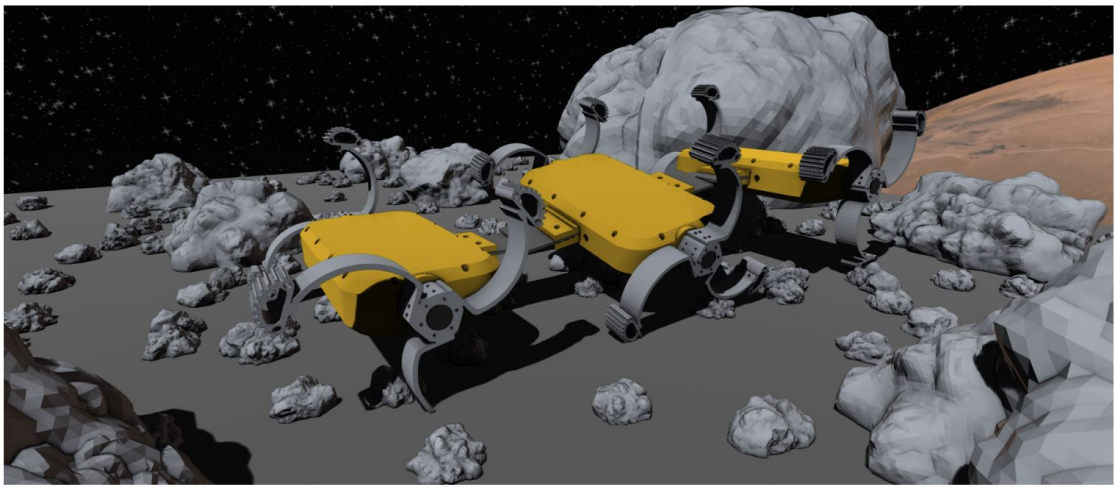

Figure 2.2.: Full SCOUT-Rover simulation in Dymola. [PL22]

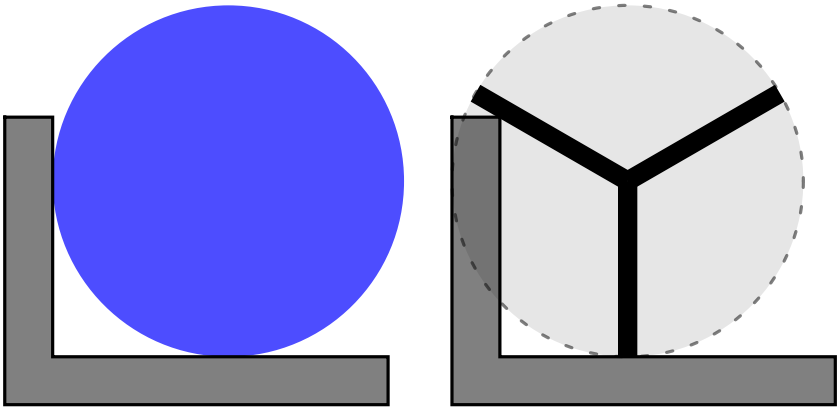

Figure 2.3.: Advantages of Rimless-Wheels with vertical offsets.

Figure 2.3, have garnered attention due to their ability to navigate vertical displacements effectively. The figure also shows that the more spokes a wheel has, the closer its behaviour approaches that of a regular wheel.

The term “Rimless-Wheel” was introduced in 1990 by Tad McGeer as an abstraction for human walking [McG90]. While McGeer’s research primarily focused on stiff spokes, which come with inherent disadvantages compared to flexible counterparts, the concept has evolved significantly since then and is now utilised in various rover designs.

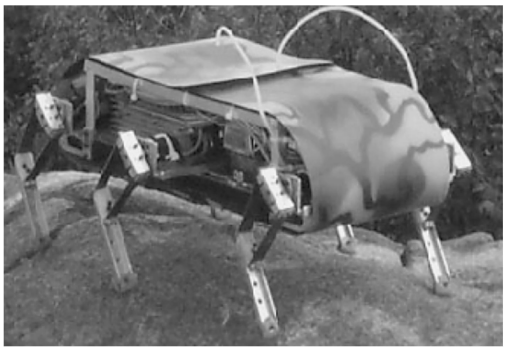

Figure 2.4.: RHex-Rover standing on rock. [A+01]

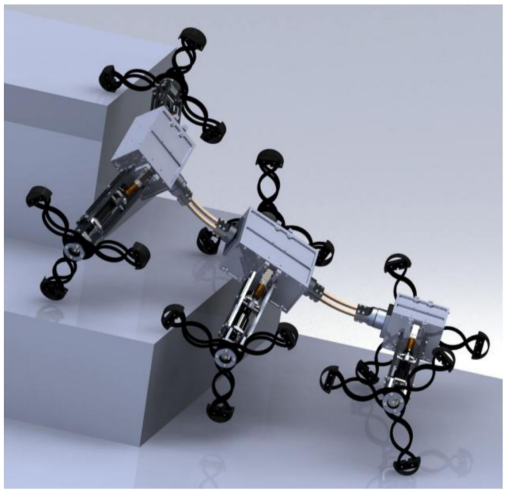

Figure 2.5.: Render of the ROLV-Rover. [MKLa11]

2.3. Rimless Wheeled Rovers

A notable application of the Rimless-Wheel concept is the RHex-Rover, depicted in Figure 2.4. This rover employs wheels consisting of single spokes rotating around a central axis, enabling smooth locomotion [A+01]. Variations of this concept have inspired multiple-spoked wheel designs, such as the Rolling Leg Vehicle (ROLV) developed in cooperation with Dr. Roy Lichtenheldt, project leader of the SCOUT-Rover [MKLa11]. The ROLV-Rover features three spokes and is segmented into three flexibly connected segments, as illustrated in Figure 2.5.

Another noteworthy example is the Coyote III, designed with a five-spoked wheel configuration for lunar and Martian exploration. This rover, depicted in Figure 2.6, emphasises "(Semi-) Autonomous operation within a logistics chain" [SAK15], with provisions for mounting a robotic arm for enhanced versatility.

In summary, Rimless-Wheel concepts represent an innovative approach to locomotion in space exploration, offering advantages in navigating challenging terrains. This section's diverse designs and applications underscore the importance of exploring alternative locomotion solutions in extraterrestrial environments.

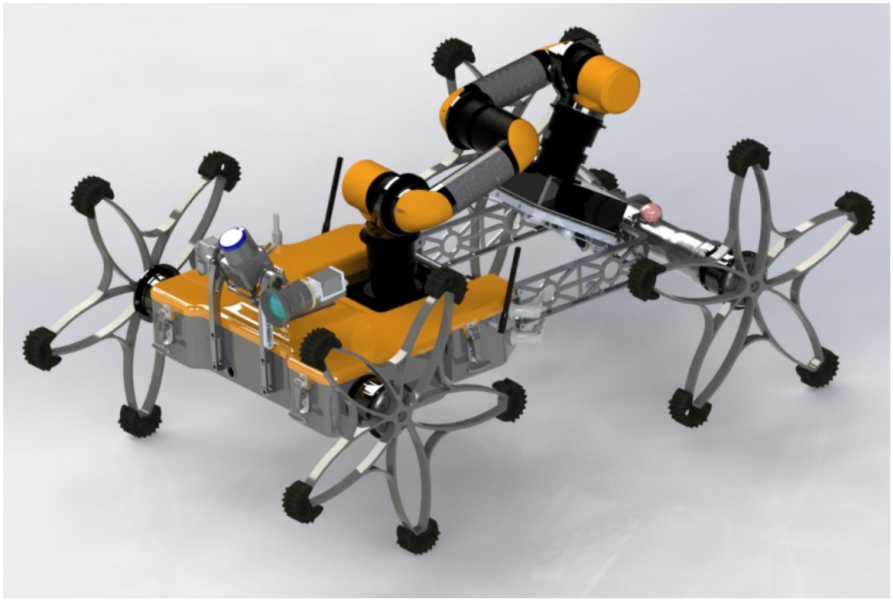

Figure 2.6.: Render of the Coyote III with robotic arm mounted [SAK15].

2.4. Contact Detection

The necessity for contact detection in machine applications arises from various factors. In medical technology, such as prostheses, and in industrial settings, such as machining, the absence of contact detection can lead to immediate damage. While the importance of contact detection in traditional wheeled applications may not be obvious, it holds significant relevance for Rimless-Wheels. Preventing damage to components due to over-stressing or unnecessary usage is engaging. Therefore, contact detection serves as useful information in ensuring the integrity and longevity of the system.
This section handles diverse approaches to contact estimation. The examination begins by exploring sensory-based methods, which use sensory inputs to recognise contact with the environment. Subsequently, applied concepts in rovers are examined, focusing on implementing contact detection in rover systems for navigating challenging terrains.

2.4.1. Sensory Technology

In modern machine applications, contact sensors provide crucial feedback for various tasks and operations. These sensors, predominantly electronic in nature, play an important role in detecting contact with the environment and ensuring the integrity of the system.

One promising technology related to contact detection is the strain-gauge sensor. Particularly prevalent in medical technology, novel strain-gauge sensors utilise interlocking platinum-coated polymer nanofibers to detect contact, shear, and torsion forces. By measuring the electric current passing through, these sensors can precisely evaluate changes in resistance, as depicted in Figure 2.7 [PLKa12].
In the context of Rimless-Wheels, integrating strain-gauge sensors into the spokes or potential contact points could detect deformation upon establishing contact, thereby enabling contact estimation.

Another approach to contact detection involves the evaluation of ultrasonic waves. By emitting ultrasonic wavefronts and analysing the reflected data, contact with the environment can be estimated. This method not only provides information on contact but also facilitates the analysis of different underground materials, as the resulting frequency varies based on the contact material [SA94]. Placing such sensors within the feet of Rimless-Wheels could offer a comprehensive contact profile, enhancing navigation capabilities in diverse terrains.

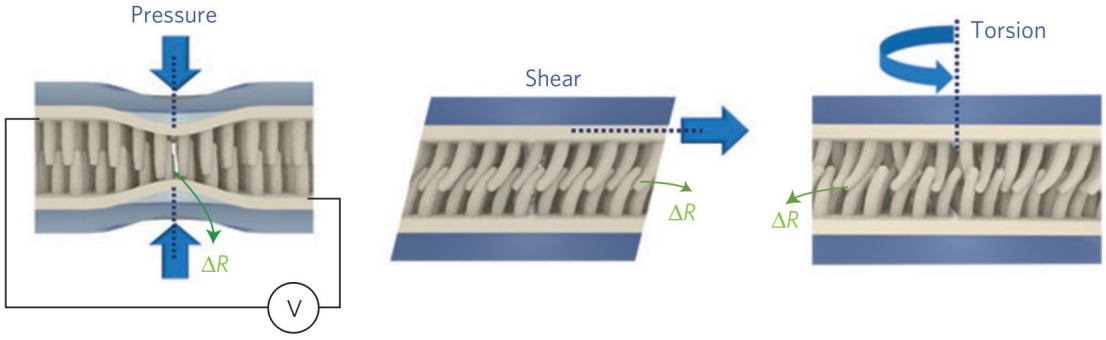

Figure 2.7.: Strain-Gauge sensor that can detect contact, shear and torsion forces. [PLKa12]

Furthermore, optical soft sensors present an innovative solution for measuring fingertip force and contact recognition. In this concept, an LED emits light through deformable Polydimethylsiloxane (PDMS) waveguides, which undergo deformation upon contact. A photodiode then detects variations in the incoming wave scheme, enabling accurate contact detection [CLKa17].
Integration of optical soft sensors within Rimless-Wheels spokes or their feet could provide valuable insights into ground contact, further enhancing the system's adaptability and performance.

2.4.2. Applied Concepts in Rovers

In the context of aerospace technologies, advancements in rover design have led to the development of innovative legged robots like the DLR-Walker. This hexapod robot, equipped with legs inspired by the design of human fingers, features three independent actuated joints in each leg, enabling omni-directional walking. The DLR-Walker can detect various environmental factors crucial for navigation by incorporating a sophisticated sensor suite, including joint position, joint torque, force torque, motor torque, and temperature sensors. Notably, using force/torque sensing enables the application of advanced soft control algorithms, facilitating smooth traversal across complex terrains. Furthermore, the DLR-Walker serves as a platform for studying navigation algorithms, empowering autonomous mapping of 3D environments. [Ari10]

In the efforts of enhanced rover mobility, researchers found answers in model-based chassis control. By incorporating terramechanics models into chassis control systems, engineers aim to optimise rover performance across various terrain types. Semi-empirical models, rooted in the work of terramechanics researchers like Bekker and Wong, offer fast and efficient simulations of wheel-ground interactions. These models, validated through rigorous testing and field trials, provide valuable insights into the forces at play during rover locomotion. Moreover, integrating wheel-ground contact effects into path-planning algorithms presents an alternative approach to enhancing rover mobility, promising more adaptive and responsive traversal strategies. [Bar20]
These advanced planning algorithms are gaining prominence in the context of rover chassis control, particularly in missions like MMX (Martian Moon Exploration) [B$^+$22]. For instance, the IDEFIX-Rover's [Lan23] operational strategy hinges on the assumption

of a predominantly flat surface, with alignment commands executed based on anticipated wheel contact angles [SBB21]. This can be observed using so-called “WheelCams”, imaging contact points of the wheels to the surface. This observation does not influence the behaviour of the rover [UMGa21]. With this estimation, a real-time contact sensor is obsolete. This approach is promising if the estimation of flat underground is true.

In the broader context of multi-terrain exploration, both wheeled and legged robots play important roles in navigating challenging environments. While wheeled robots excel on smooth surfaces, legged robots offer superior mobility in rough terrain by adapting to surface irregularities through discrete footholds. Closed-loop gait planning designs leverage sophisticated sensing elements and adaptive algorithms to navigate diverse terrains effectively. For example, RiSE uses joint position sensors, leg strain sensors and foot contact sensors in each one of its six legs. Additionally, innovative Wheg (legged wheel) designs featuring curved leaves enhance static stability and reduce torque requirements, improving endurance and performance in challenging environments. [ADMa16]

While all of these approaches are sensibly chosen for their respective rover types, the SCOUT-Rover cannot meaningfully adapt any of these concepts. Compared to the other rover concepts mentioned above, the SCOUT-Rover is designed to be robust and efficient. Any additional sensor technology is therefore unsuitable. A new concept must be developed that only uses the sensor data of the motor controller. The basic concept of contact detection and the calculations required for this are derived in the following Chapter 3.

3. Modelling

Constructing a mathematical model necessitates preliminary considerations in order to balance simplicity and comprehensiveness. To represent the relevant effects, the accuracy and the quality of the model depend on the right choice of required parameters. This chapter includes the model assumptions, the definition of a coordinate system and the derivation of the model. Furthermore, the contact detection strategy is explained, and the outcome of a protocol is set into perspective.

3.1. Assumptions

The dynamics of a simplified wheel are discussed, with the coordinate origin set at its axis of rotation.
In this study, a non-elastic system is examined. Consequently, every component and object interacting with it is treated as rigid. Considering elastic systems, while being generally important, do not significantly impact the outcome of this study.
Thermal effects, such as the expansion of mechanical parts or heat generation due to friction, are excluded from consideration. Although they influence the model's dynamics, their impact is minimal, and including them would unnecessarily complicate matters.
At the low RPM at which the wheel operates, air friction is negligible [GZZa23] and therefore not considered.
However, one frictional aspect that requires attention is within the gearbox. The datasheet provides an efficiency coefficient for this friction [Max21b]. If the coefficient is less than 100%, mechanical energy dissipates as heat. Given the exclusion of thermal effects, this results in an energy deduction factor. According to [PSO02], this gearbox friction can be approximated as linear, making it feasible to examine. Its significance becomes relevant in the following section.

Another friction that can not be neglected is the friction between the wheel and the ground. Here, it is assumed that a foot that established ground contact can not slip on it.
Additionally, the process of data transmission is simplified. The communication between the electrical motor, motor controller and computer is assumed to be instantaneous and free of data loss. The motor model is also simplified so that inductance and resulting effects are neglected. Also the exact internal electronic structure is simplified.

Dimension Parameters:

Accurate parameters of the rover's weight were obtained through several measurements to validate its specifications. To ensure that reproducible results can be derived from the model, the dimensional parameters of the rover have to be precise. Given the ongoing development process, components undergo regular updates, rendering the information in Table 2.1 potentially outdated. For example, the current total mass of the rover was determined to be approximately 20.001 kg. These measurements were conducted to ascertain the weights of the wheel components, the rover itself, and the load carried by each individual leg. The detailed results are provided in the appendix in Protocol B.

3.2. Theoretical Free Wheel Case

In this scenario, the wheel rotates freely without making contact with the ground. The variables of interest include the time-dependent rotation angle $\varphi(t)$, its derivatives and the current I.
Given the triangular symmetry of the SCOUT Rimless-Wheel and the absence of interaction with other objects, the model can be simplified. This symmetry is illustrated in Figure 3.1, where the dotted lines represent axes of symmetry, and the coordinate origin is denoted as θ.
The simplified wheel resulting from this analysis is depicted in Figure 3.2. The left schematic highlights the cylindrical structure and fundamental radii. The cross-section shown on the right-hand side, reveals consistent thickness and equal diameters for each cylinder. Specifically pointing out, a simplified wheel consists of one full cylinder Z_1 and two hollow cylinders Z_2 and Z_3.
Z_1 corresponds to the wheel mounting constructed from aluminium. Z_2 represents the

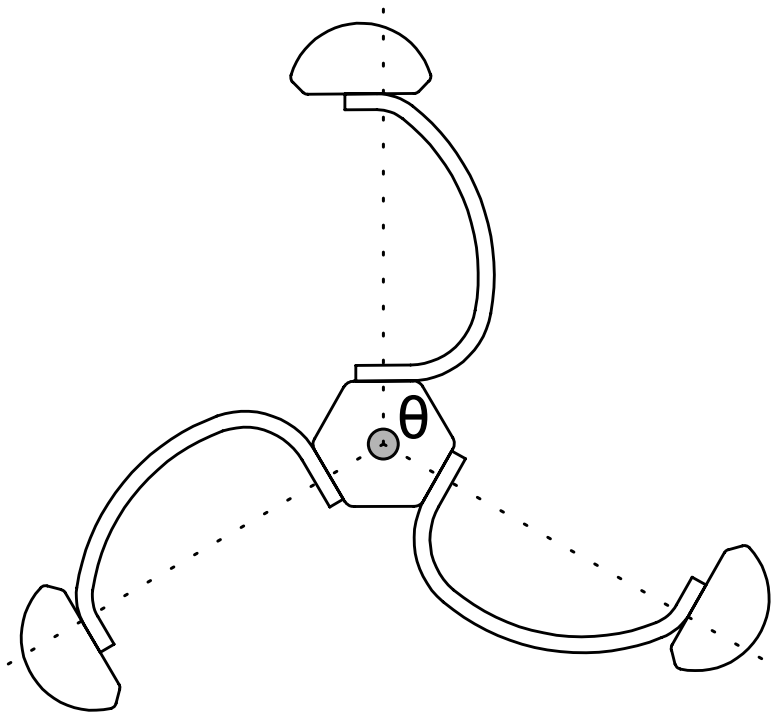

Figure 3.1.: View of real Rimless-Wheel with symmetry point and coordinate origin.

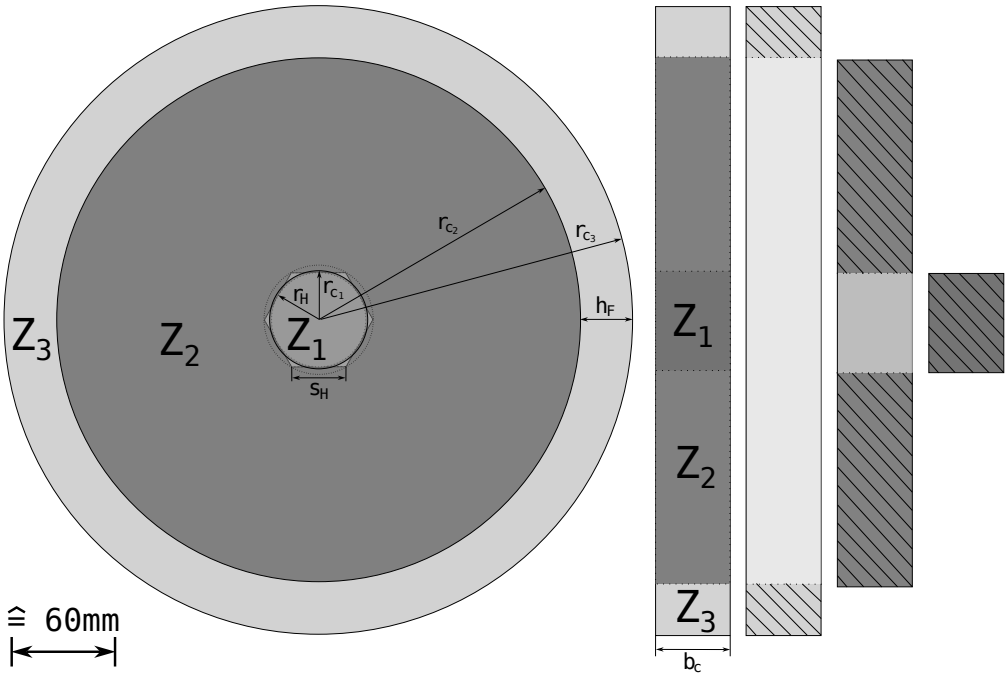

Figure 3.2.: Simplified wheel composed of several cylinders.

Wheel width	b_c	44.1	mm
Hexagon height	d_H	55.0	mm
Length of spoke	l_S	125.0	mm
Height of foot	h_F	30.5	mm

Table 3.1.: Rimless-Wheel measurements.

wheel spokes, out of POM (Polyoxymethylene), a plastic initially cast and then machined into shape. Finally, Z_3 represents the feet of the wheel, made from a rubbery 3D-printer filament called TPU (Thermoplastic Polyurethane).
All cylinders rotate around the same axis at identical angular velocities $\omega(t)$. By determining their respective radii r_{c_i}, weights m_i, and width b_c, where $i \in \{1, 2, 3\}$ a formula for the total mass inertia J_{tot} can be derived.
The values presented in Table 3.1 were obtained during the measurements of the weights in Protocol B, using a calliper capable of precise measurements down to a hundredth of a millimetre with a tolerance of 0.2%. To ensure measurements, they were cross-referenced with the CAD model of the Rimless-Wheel. With the dimensional parameters set, the calculation of the geometric relations of the wheel can be carried out.

Full Cylinder Z_1:

At this stage, the shape of the wheel mount is idealised to form a perfect hexagon. Although the actual shape is more complex, as illustrated in Figure 3.1, this simplification does not significantly impact the argumentation. With the inner diameter denoted as d_H, the side length of the hexagon s_H and its area A_H are given by

$$\begin{aligned} s_H &= \tfrac{\sqrt{3}}{3} d_H &&= 28.7 \text{ mm}, \\ A_H &= \tfrac{3\sqrt{3}}{2} {s_H}^2 &&= 2584.7 \text{ mm}^2. \end{aligned} \tag{3.1}$$

This is used to construct a circle with the same area as the hexagon $A_H = A_{c_1} = \pi {r_{c_1}}^2$. The radius

$$r_{c_1} = \sqrt{\frac{A_H}{\pi}} = 28.7 \text{ mm}$$

of this circle is subsequently employed to calculate the dimensions of the other cylinders.

Hollow Cylinder Z_2:

Using the measured values of l_S, the smallest distance between the foot and the inner cylinder is determined. This length represents a straight and simplified spoke length. The hollow cylinders Z_2 parameters are given by

$$\begin{aligned} r_{c_2} &= l_S + \tfrac{d_H}{2} &&= 152.5 \text{ mm}, \\ r_{c_{12}} &= r_{c_2} - r_{c_1} &&= 123.8 \text{ mm}, \\ A_{c_{12}} &= \pi \left(r_{c_r}^2 - r_{c_1}^2\right) &&= 70477.0 \text{ mm}^2. \end{aligned} \tag{3.2}$$

Hollow Cylinder Z_3:

Similarly to (3.2), these necessary parameters can be calculated as

$$\begin{aligned} r_{c_3} &= r_{c_2} + h_F &&= 183.0 \text{ mm}, \\ A_{c_{23}} &= \pi \left(r_{c_3}^2 - r_{c_2}^2\right) &&= 32147.0 \text{ mm}^2, \end{aligned} \tag{3.3}$$

using the measured value of the foot height $h_F = r_{c_{23}}$.

The derived cylinder base areas and radii facilitate the computation of the individual mass moments of inertia.

3.2.1. Mass Moments of Inertia

The mass moment of inertia is a fundamental concept in mechanical engineering. While determining the mass moment of inertia for certain objects can be challenging [PAAa16], in this case, assumptions are employed to simplify the calculation of the mass moments of inertia J_i, for $i \in \{1, 2, 3\}$. Here, it is assumed that the mass m_i, radius r_{c_i}, and density ρ_i of each cylinder Z_i is constant, for $i \in \{1, 2, 3\}$, and that the rotation axis is situated at the centre for all cylinders. Generally, the mass moment of inertia is given by

$$J = \int_{Z_i} \|\mathbf{r}_\perp\|^2 \rho(\mathbf{r}) \, dV_c, \tag{3.4}$$

where $\rho(\cdot)$ is the mass density function at each point $\mathbf{r}$ and $\mathbf{r}_\perp$ is a perpendicular vector to the rotational axis, from which it extends to $\mathbf{r}$. The integration with respect to the cylindrical volume V_c is evaluated for the cylinder Z_i.

Under the previously stated assumptions $\rho(\mathbf{r}) = \rho = \frac{m}{b_c A}$ and

$$dV_c = b_c \, dA = 2\pi b_c r \, dr, \tag{3.5}$$

which yields

$$\begin{aligned} J_i &= \int_{r_{c_{i-1}}}^{r_{c_i}} r^2 \frac{m_i}{b_c A_i} 2\pi b_c r \, dr = 2\pi \frac{m_i}{A_i} \int_{r_{c_{i-1}}}^{r_{c_i}} r^3 \, dr = 2\pi \frac{m_i}{A_i} \left[\frac{r^4}{4} \right]_{r_{c_{i-1}}}^{r_{c_i}} \\ &= 2\pi \frac{m_i}{\pi({r_{c_i}}^2 - {r_{c_{i-1}}}^2)} \frac{{r_{c_i}}^4 - {r_{c_{i-1}}}^4}{4} = \frac{m_i}{2} \left({r_{c_i}}^2 - {r_{c_{i-1}}}^2 \right). \end{aligned} \tag{3.6}$$

Note that r_{c_0} is set to zero.

Also supported by the work of [PAAa16], it can be seen that for cylinders with the previous assumptions, the following equation is obtained:

$$J_Z = \frac{m_Z}{2}(r_o^2 - r_i^2). \tag{3.7}$$

Where r_o is the outer radius, and r_i is the inner radius of a hollow cylinder. Though Protocol B, the masses of the wheel mounting, the spokes and the feet were determined and the results are summarised in Table 3.2[1]. Note that there are three spokes and three feet per wheel, therefore, their mass value has to be multiplied by three to obtain the correct weight.
It is worth mentioning that no screws, nuts or washers are considered here. This results in a difference of $\Delta m = 0.0578$ kg. Since modelling these parts separately would not improve the model a lot, their weight is neglected.

[1] Tolerances are given in Protocol B

Wheel mounting	m_M	0.248	kg
Spokes	m_S	0.203	kg
Feet	m_F	0.027	kg

Table 3.2.: Weight of Rimless-Wheel components.

With the masses, the individual mass moments of inertia can be calculated:

$$\begin{aligned} J_1 &= \tfrac{m_M}{2}(r_{c_1} - r_{c_0}) = 1.0194 \cdot 10^{-4} \text{ kg m}^2, \\ J_2 &= \tfrac{m_S}{2}(r_{c_2} - r_{c_1}) = 22.748 \cdot 10^{-3} \text{ kg m}^2, \\ J_3 &= \tfrac{m_F}{2}(r_{c_3} - r_{c_2}) = 4.1443 \cdot 10^{-3} \text{ kg m}^2. \end{aligned} \tag{3.8}$$

Summing up the individual inertia yields

$$J_\text{W} = J_1 + J_2 + J_3 = 2.7911 \cdot 10^{-3} \text{ kg m}^2. \tag{3.9}$$

An integral component of the system is the planetary gearbox with a transmission ratio of 66 : 1 [Max21b]. The gear transmission factor denoted as $\iota = 66$, serves as an essential parameter for transforming gearbox inputs into corresponding outputs. Every angular change $\Delta\varphi(t)$, is reduced by a factor of ι, concurrently amplifying the torque by a multiplication factor of ι, resulting in the relations

$$\varphi_\text{W}(t) = \frac{\varphi_\text{M}(t)}{\iota}, \quad \frac{d}{dt}\varphi_\text{W}(t) = \omega_\text{W}(t) = \frac{\omega_\text{M}(t)}{\iota}, \quad \frac{d}{dt}\omega_\text{W}(t) = \alpha_\text{W}(t) = \frac{\alpha_\text{M}(t)}{\iota}. \tag{3.10}$$

The gearbox efficiency, denoted as $\eta_\text{GB} = 0.72$, implies that only 72% of the input rotational energy is converted into output rotational energy and vice versa [Max21b]. It can be assumed that the loss in energy concerns heat generation due to internal friction. The thermal effects are, therefore, neglected. The gearbox itself has a mass moment of inertia itself: $J_\text{GB} = 15 \cdot 10^{-6}$ kg m^2. [Max21b]

Electric Motor:

The brushed direct current (DC) motor operates under a constant battery voltage of $V_\text{B} = 48$ V. Its datasheet states an inner resistance of $R_\text{M} = 1.13\ \Omega$ [Max22]. Neglecting induction effects, which have a reaction time in the millisecond range, the system simplifies to a basic circuit comprising only a resistor in series with a voltage source. According to Kirchhoff's law of currents

$$I_1 = I_2 = \ldots = I_n$$

for $n \in \mathbb{N}$, the current remains constant, while Ohm's law states that $V = R \cdot I$. This allows the calculation of the voltage.
Emphasising the significance of the potential resistance $R_\text{P}(t)$ is important as it enables

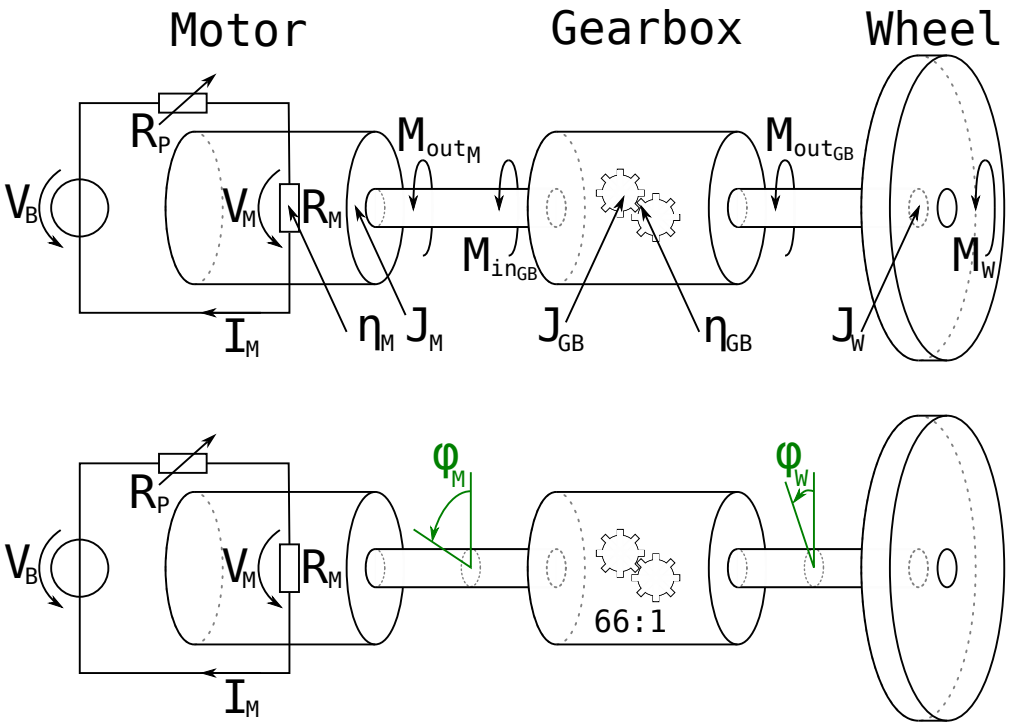

Figure 3.3.: Simplified view on the drive chain.

current regulation. Although the real motor controller includes more functionalities than merely controlling a resistor, this simplification suffices for the present consideration. The motor current

$$I_{\mathrm{M}} = \frac{V_{\mathrm{B}}}{R_{\mathrm{P}}(t) + R_{\mathrm{M}}}$$

is, therefore, dependent on both the internal resistance of the motor and the variable motor controller resistance. Additionally, the motor datasheet specifies the mass moment of inertia as $J_{\mathrm{M}} = 137 \cdot 10^{-6}$ kg m^2. [Max22]

3.2.2. Torque Computation

The schematic representation in Figure 3.3 illustrates the comprehensive model, tracing from the electrical input through the gearbox into the wheel. This depiction aims to clarify the composition of the subsequent torque computation process.

Remark: When computing rotational torque, it is essential to consider a rotational system. Usually, the unit [rad], denoting rotation around a rotational axis, is implied rather than explicitly stated. However, in this analysis, it is retained, underscoring how individual steps contribute to the overall computation. In addition, time dependencies are not always written out in order to maintain readability.

A general formula to calculate a rotational torque M is given in the following equation:

$$M = J\alpha(t), \qquad M : 1\left[\mathrm{kg\,m^2}\right]\left[\frac{\mathrm{rad}}{\mathrm{s^2}}\right] = 1\left[\mathrm{Nm\,rad}\right]. \tag{3.11}$$

This equation addresses the primary concern yet neglects the influence of friction. Introducing friction into the system is essential for realism, with the gearbox efficiency η_{GB} providing the means to account for it. This necessitates an understanding of friction energy

$$E_R = (1-\eta)\left(\frac{1}{2}J\omega(t)^2\right), \qquad E_R : 1\left[\mathrm{kg\,m^2}\right]\left[\frac{\mathrm{rad^2}}{\mathrm{s^2}}\right] = 1\left[\mathrm{Nm\,rad^2}\right]. \tag{3.12}$$

Notably, upon closer examination, it becomes apparent that the units of Equations (3.11) and (3.12) do not align. Fortunately, a crucial step remains to convert this energy into torque. By the law of energy conservation, the rotational work W_R represents a change in kinetic energy. Since the angular velocity $\omega(t)$ is a time variable, changes that occur during accelerations are recognised, resulting in the following relation:

$$W_R = \Delta E_R = \tfrac{1}{2}J\omega(t)^2. \tag{3.13}$$

When divided by the angle φ, the desired frictional torque M_R can be derived. If a perfect energy conversion efficiency would occur, it would yield a value of one. If that happens, the friction torque would be zero. If this connection is taken into account, then the factor $(1-\eta)$ has to be included. Equation (3.14) presents this and serves to confirm that M_R now possesses the correct units:

$$M_R = \frac{W_R}{\varphi(t)} = \frac{(1-\eta)}{2}\frac{J\,\dot{\varphi}(t)^2}{\varphi(t)}, \qquad M_R : 1\left[\frac{\mathrm{Nm\,rad^2}}{\mathrm{rad}}\right] = 1\left[\mathrm{Nm\,rad}\right]. \tag{3.14}$$

However, a crucial point remains unresolved: determining the appropriate value for J in this scenario, given the existence of multiple mass moments of inertia. While the gearbox specifies its own moment of inertia, it does so without specifying whether it

refers to the input or output. Consequently, it is assumed that the specified moment of inertia corresponds to the input, establishing the following relationship:

$$\begin{aligned} M_{\mathrm{W}} &= J_{\mathrm{W}}\,\ddot{\varphi}_{\mathrm{W}}(t), \\ M_{\mathrm{GB}} &= J_{\mathrm{GB}}\,\ddot{\varphi}_{\mathrm{M}}(t) \overset{(3.10)}{=} J_{\mathrm{GB}}\,\iota\,\ddot{\varphi}_{\mathrm{W}}(t), \\ M_{\mathrm{M}} &= J_{\mathrm{M}}\,\ddot{\varphi}_{\mathrm{M}}(t) \overset{(3.10)}{=} J_{\mathrm{M}}\,\iota\,\ddot{\varphi}_{\mathrm{W}}(t). \end{aligned} \tag{3.15}$$

In Equation (3.15), every angle is transformed into $\ddot{\varphi}_{\mathrm{W}}(t)$, as the system is analysed from the wheel's standpoint. Given that M_{M}, M_{GB}, and consequently M_{R} are already correctly scaled, the system's total torque

$$M_{\mathrm{tot}} = M_{\mathrm{W}} + M_{\mathrm{GB}} + M_{\mathrm{M}} = \ddot{\varphi}_{\mathrm{W}}(t)\,\underbrace{\iota\left(\frac{J_{\mathrm{W}}}{\iota} + J_{\mathrm{GB}} + J_{\mathrm{M}}\right)}_{=:\,J_{\mathrm{tot}}} \tag{3.16}$$

results. The equation for the target free wheel torque M_{des_f} can be derived subsequently

$$M_{\mathrm{des}_f} = M_{\mathrm{tot}} + M_{\mathrm{R}} = J_{\mathrm{tot}}\,\iota\left(\ddot{\varphi}_{\mathrm{W}}(t) + \frac{(1-\eta_{\mathrm{GB}})}{2}\frac{\dot{\varphi}_{\mathrm{W}}(t)^2}{\varphi_{\mathrm{W}}(t)}\right) \tag{3.17}$$

as the sum of the systems total and frictional torque.

3.2.3. Free Wheel Motor Current

The concept of power, representing the transfer of energy over time, is fundamental in physics and is commonly expressed as $P = F\,v$, where F denotes force and v denotes velocity.
For rotational systems, power can be defined as $P_{\mathrm{rot}} = M\,\omega(t)$, where M represents torque and $\omega(t)$ represents angular velocity. In the context of electrical systems, power is typically expressed as $P_{\mathrm{el}} = I \cdot V$, where I denotes electrical current measured in amperes and V denotes electrical potential difference measured in volts. The unit of every power is measured in watts, allowing for the transformation $P_{\mathrm{el}} = P_{\mathrm{rot}}$ expressed in terms of

$$I \cdot V = M\,\omega(t). \tag{3.18}$$

For the free wheel case, this results in the rotational power

$$P_{\mathrm{rot}_f} = M_{\mathrm{des}_f}\,\dot{\varphi}_{\mathrm{M}}(t) = M_{\mathrm{des}_f}\,\iota\,\dot{\varphi}_{\mathrm{W}}(t). \tag{3.19}$$

The motor efficiency denoted as $\eta_{\mathrm{M}} = 0.92$ implies that approximately 92% of the electrical energy is converted into rotational energy [Max22]. While the datasheet lacks information about internal friction, the assumption is made that the energy loss solely arises from electrical components converting electrical energy into thermal energy. Although this assumption may oversimplify the system, it provides a reasonable approximation for modelling purposes. Considering the effect of the motor efficiency $\eta_M = 0.92$, the electrical power reduces to

$$P_{\mathrm{el}_f} = \frac{P_{\mathrm{rot}_f}}{\eta_M} \overset{(3.19)}{=} \frac{M_{\mathrm{des}_f}\,\iota\,\dot{\varphi}_{\mathrm{W}}(t)}{\eta_M}. \tag{3.20}$$

Given a constant battery voltage $V_{\mathrm{B}} = 48$ V, rearranging yields

$$I_{\mathrm{M}_f}(t) = \frac{P_{\mathrm{rot}_f}}{V_{\mathrm{B}}} = \frac{M_{\mathrm{des}_f}\,\iota\,\dot{\varphi}_{\mathrm{W}}(t)}{\eta_M\,V_{\mathrm{B}}} \tag{3.21}$$

to derive an explicit formula for the free wheel current $I_{\mathrm{M}_f}(t)$.

3.3. Theoretical Contact Case

In the contact scenario, the analysis focuses on the interaction between a single foot and the ground. Consequently, the wheel mounting is now represented by an extruded hexagon, offering a more detailed depiction. The spokes are conceptualised as slender rods with a uniform diameter, signifying the distance between the actual wheel mounting and the rubber feet. Moreover, these feet are abstracted into extruded half circles, with their radii representing the dimensions of the authentic foot. The process of abstraction is illustrated in Figure 3.4. The previous Section 3.2 explains the dynamics of motor and gearbox, which will remain unchanged for this chapter.

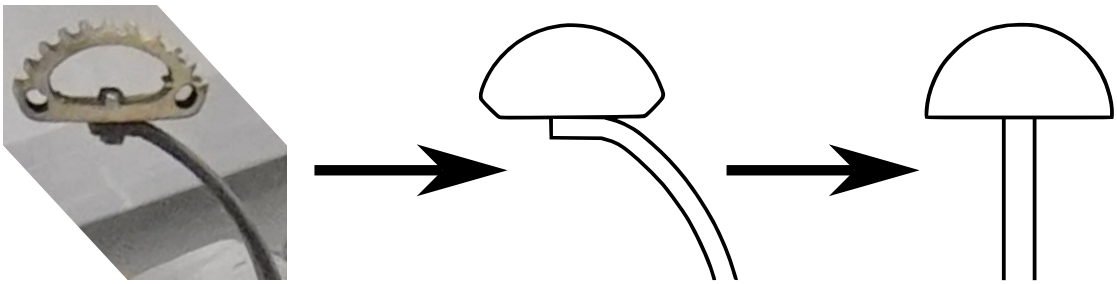

Figure 3.4.: Abstraction steps for rubber foot.

3.3.1. Contact Vector

The evolved wheel structure no longer has a constant radius and therefore complex contact points are to be expected. The rotation angle, denoted as φ, remains in this context. However, it necessitates a reference point, which is provided by a designated foot highlighted with dark green outlines. When the centre of this foot aligns with the z-axis, φ assumes a value of 0. This is illustrated in the upper left corner of Figure 3.5.

In the context of calculating the contact point, establishing a coherent coordinate system is important. Here, the coordinate origin, denoted as θ, is positioned at the centre of the hexagon. The angle φ denotes the rotation around the y-axis, with the assumption that the wheel remains fixed in its y-position. Notably, during the wheel's rotation in a positive mathematical sense, it is not displaced along the negative x-axis but maintains its x-position. This assumption aligns with the absence of slippage on the ground, implying that a wheel in contact with the ground invariably traverses the surface beneath it. Consequently, the wheel remains fixed relative to the z-axis, with any rotational displacement observed concerning the ground.
Vector-based calculations are instrumental in determining the contact point, with the primary vector of interest being denoted as $\boldsymbol{\vartheta}$. This vector is formed through a summation of various vectors pointing towards significant points. Given that a straight line can be drawn to the ground, intersecting the ground plane orthogonally, a right angle at $\gamma = 90°$ can be identified. Leveraging the fact that the sum of angles in a triangle totals 180°, additional angles within the triangle can be expressed as

$$\begin{aligned} \alpha + \beta + \gamma = 180° \wedge \gamma = 90° \quad &\Longrightarrow \quad \alpha + \beta = 90° \\ &\Longrightarrow \quad \beta = 90° - \alpha. \end{aligned} \tag{3.22}$$

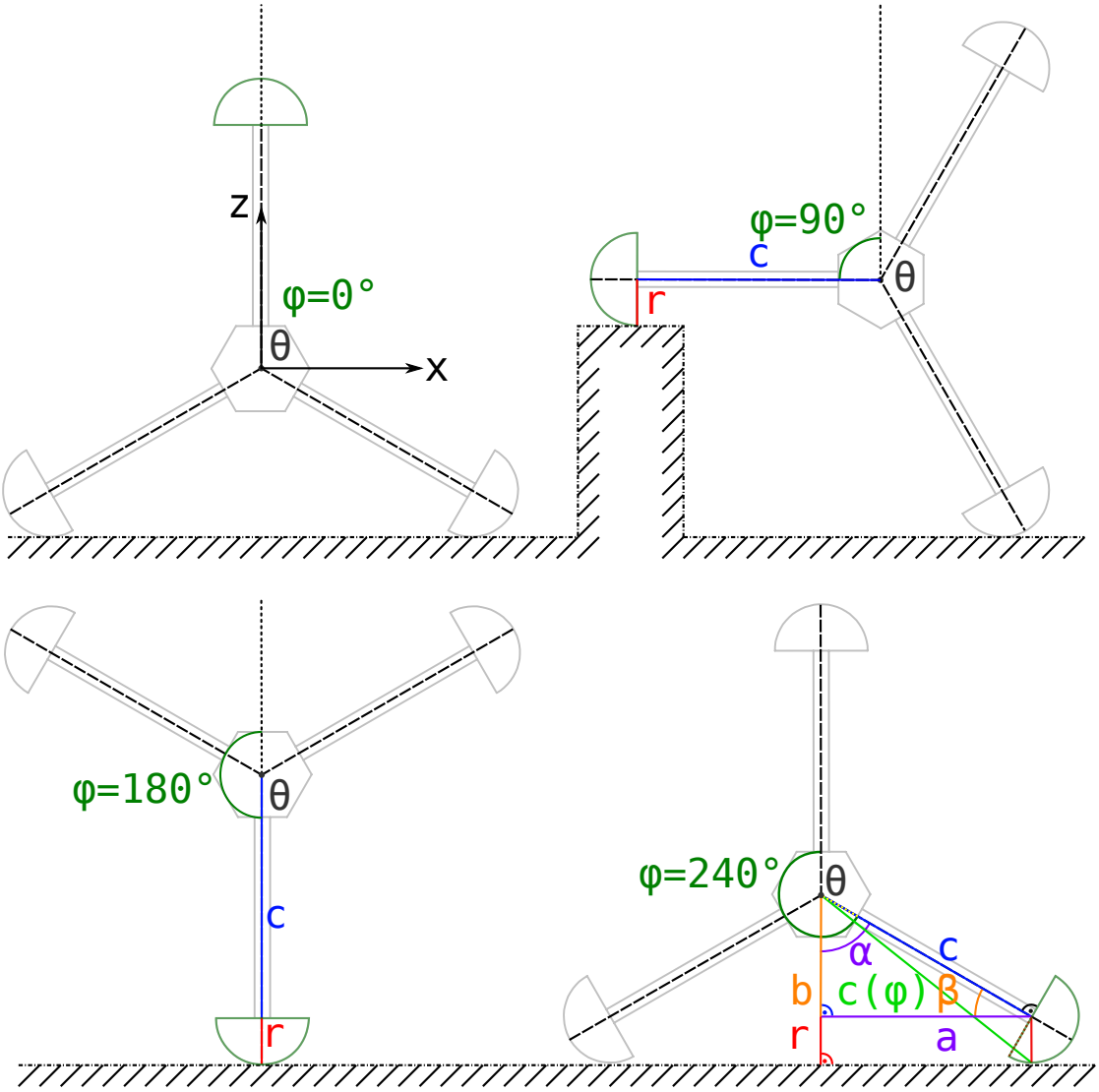

Figure 3.5.: Four different wheel orientations.

With the correlation between α and φ, the following equations can be described exclusively in terms of φ. This relation can further be observed in Figure 3.5 in the lower left corner. As $\alpha = 0°$ when $\varphi = 180°$, the implication

$$\alpha = \varphi - 180° \quad \Longrightarrow \quad \beta = 270° - \varphi \tag{3.23}$$

is obvious. The distance from the coordinate centre to the centre of the foot

$$l = r_i + l_S = 125 \text{ mm} + 27.5 \text{ mm} = 152.5 \text{ mm}$$

consists of sum of the inner circle radius $r_i = \frac{d_H}{2}$ of the hexagon and the simplified spoke length l_S.

Considering the Law of Sines, the constant wheel diameter vector

$$\boldsymbol{\vartheta}_l = \begin{bmatrix} l \sin(\alpha) \\ -l \sin(\beta) \end{bmatrix} \overset{(3.23)}{=} \begin{bmatrix} -l \sin(\varphi) \\ l \cos(\varphi) \end{bmatrix} \tag{3.24}$$

can be formed. Another occurring vector is

$$\boldsymbol{\vartheta}_r = \begin{bmatrix} 0 \\ -r \end{bmatrix}, \tag{3.25}$$

which is always orthogonal to the ground, ensuring that its x-component remains constantly zero. As the foot is modelled as a semicircle, its z-module maintains a consistent radius throughout the interval of interest

$$90° \leq \varphi \leq 270°.$$

In Figure 3.5, four distinct scenarios of wheel orientation are shown. In the upper left corner, a wheel with no rotation is illustrated, corresponding to $\varphi = 0°$. Adjacent to the coordinate centre θ, a wheel is tilted at 90°, representing the considered lower limit of orientation. Further rotation would lead to the wheel climbing. Below, a case with $\varphi = 240°$ is depicted, illustrating the composition of the contact vector $\boldsymbol{\vartheta}(\varphi)$. Additionally, a wheel positioned on one leg is portrayed, corresponding to $\varphi = 180°$.

Combining (3.24) and (3.25) the desired vector

$$\boldsymbol{\vartheta}(\varphi) = \boldsymbol{\vartheta}_l + \boldsymbol{\vartheta}_r = \begin{bmatrix} -l\,\sin(\varphi) \\ l\,\cos(\varphi) - r \end{bmatrix} \tag{3.26}$$

can be derived. With Equation (3.26), the distance $c(\varphi)$ from the centre of the wheel to the contact point can be calculated. For that, the absolute value

$$|\boldsymbol{\vartheta}(\varphi)| = c(\varphi) = \sqrt{(-l\,\sin(\varphi))^2 + (l\,\cos(\varphi) - r)^2} \tag{3.27}$$

is calculated.

3.3.2. Gravity Effects

The influence of gravity is significant for a rover. It exerts a gravitational force, denoted as $\mathbf{F}_g = m \cdot g$, where m represents the object's mass and $g \approx 9.81\,\mathrm{m\,s^{-2}}$ denotes the acceleration due to gravity on Earth. Figure 3.6 illustrates an example of a one-legged scenario, showcasing the orientation of gravity and its corresponding force.

The number of spokes n_S is three for the current version of the SCOUT's Rimless-Wheel. This is important since the behaviour of a Rimless-Wheel changes drastically with the number of spokes [McG90]. The spokes are separated by an equal angle $\upsilon = \frac{2\pi}{n}$. For an initial standing position of a left spoke $\upsilon_{S_{\text{init}}}$ and for the angle of the standing spoke υ_S as shown in Figure 3.6, the following

$$\upsilon_{S_{\text{init}}} = \pi - \tfrac{\upsilon}{2}, \qquad \upsilon_S = \upsilon_{S_{\text{init}}} + \varphi_W \bmod \upsilon \tag{3.28}$$

holds. The torque required to counteract the gravitational pull on the SCOUT-Rover is calculated as follows

$$M_g = M_g(\upsilon_S) = c(\upsilon_S)\,\frac{\mathbf{m}_{\text{SCT}}}{Q_i}\,g\,\sin\left(\arctan 2\left((b(\upsilon_S) + r), a(\upsilon_S)\right) - \frac{\pi}{2}\right), \tag{3.29}$$

using its mass $\mathbf{m}_{\text{SCT}}$. Equation (3.29) comprises the $\arctan 2$ function, a two-argument $\arctan(\cdot)$, which is the inverse function of the regular trigonometric function $\tan(\cdot)$. It describes the measured angle in radians between the x-axis and a vector from the origin θ to a point (x, z). Since using the regular $\arctan\left(\frac{b+r}{a}\right)$ could result in a division by zero,

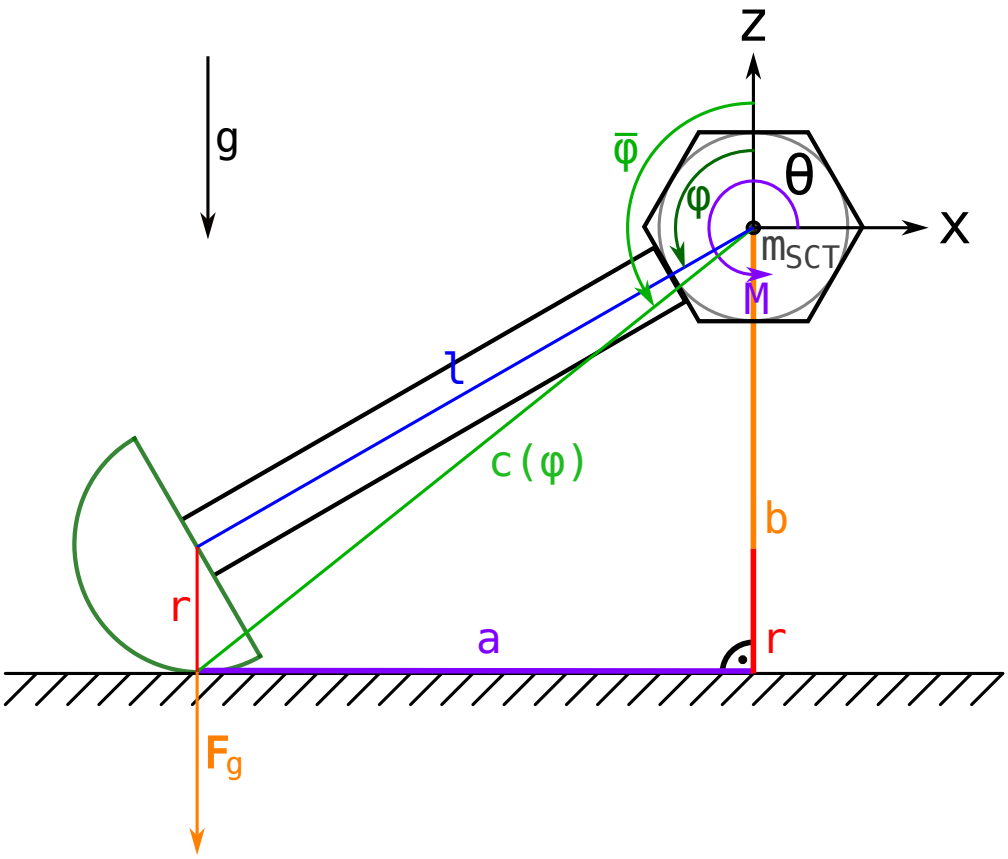

Figure 3.6.: Gravity effects on the wheel.

this approach is superior. As the wheel rotates through its cycle, the sine function alone wouldn't fully capture the discrete changes in torque at specific rotational positions in the Rimless-Wheel. The arctan 2 function effectively delineates these transitions with the use of the modulus, thereby creating distinct intervals where the torque undergoes abrupt changes. It is, therefore, ensured that the sine function resets periodically at multiples of $\frac{2\pi}{n}$ radians. This operation effectively marks the points where the torque transitions from its maximum to its minimum values and vice versa, aligning with the Rimless-Wheel's rotational symmetry, capturing the discrete nature of the torque variation throughout the wheel's rotation, enabling a precise representation of its dynamic behaviour. It is important to note that this approach still represents a simplification that assumes that there is no slipping between the feet and the ground and therefore cannot fully simulate the behaviour of a wheel in contact with the ground.

Since only one motor is currently observed, it is reasonable to assume that each motor supports only a fraction $Q_i, i \in \{1, \ldots, 6\}$ of the total mass of the rover. These fractions have been determined through tests outlined in Protocol B, where the weight distribution for each segment was examined. Depending on the segment, the appropriate weight fraction for each motor must be selected. By combining the gravitational torque with the torque considerations outlined in the previous Section 3.2, an initial estimate for the contact torque

$$M_{\mathrm{des}_c} = M_{\mathrm{des}_f} + M_{\mathrm{g}} \tag{3.30}$$

can be obtained. This torque can further be substituted to formulate the desired contact motor current

$$I_{\mathrm{M}_c}(t) = \frac{P_{\mathrm{rot}_c}}{V_{\mathrm{B}}} = \frac{M_{\mathrm{des}_c}\, \iota\, \dot{\varphi}_{\mathrm{W}}(t)}{\eta_M\, V_{\mathrm{B}}}. \tag{3.31}$$

3.4. Contact Detection Logic

To construct a comprehensive model, an algorithm must be developed to distinguish between wheel ground contact and no contact. This algorithm further referred to as Calculated-Detection, relies on the measured values of the actual motor current $I_{\mathrm{M_r}}$. With this value known, the algorithm is constructed. For that, the average values $\mathbb{A}_f$ or $\mathbb{A}_c$ are evaluated. These average values observe a time horizon $h_t \in \mathbb{N}$ around a point in time t_i, $i \in \{1, \ldots, n\}, n \in \mathbb{N}$ and the absolute of the difference between $I_{\mathrm{M}_r}(t_i)$ and $I_{\mathrm{M}_f}(t_i)$ or $I_{\mathrm{M}_c}(t_i)$. These differences are summed up for all values, resulting in

$$\begin{aligned} \mathbb{A}_f(t_i) &= \frac{1}{2h_t} \sum_{j=-h_t}^{h_t} \left| I_{\mathrm{M}_r}(t_i + j) - I_{\mathrm{M}_f}(t_i + j) \right|, \\ \mathbb{A}_c(t_i) &= \frac{1}{2h_t} \sum_{j=-h_t}^{h_t} \left| I_{\mathrm{M}_r}(t_i + j) - I_{\mathrm{M}_c}(t_i + j) \right|. \end{aligned} \tag{3.32}$$

This assessment requires access to information about φ_W and its derivatives, since the Equations (3.21) for $I_{\mathrm{M}_f}(t)$ and (3.31) for $I_{\mathrm{M}_c}(t)$ necessitate these values. If the estimated free wheel average $\mathbb{A}_f$ is smaller than the estimated contact average $\mathbb{A}_c$, the boolean

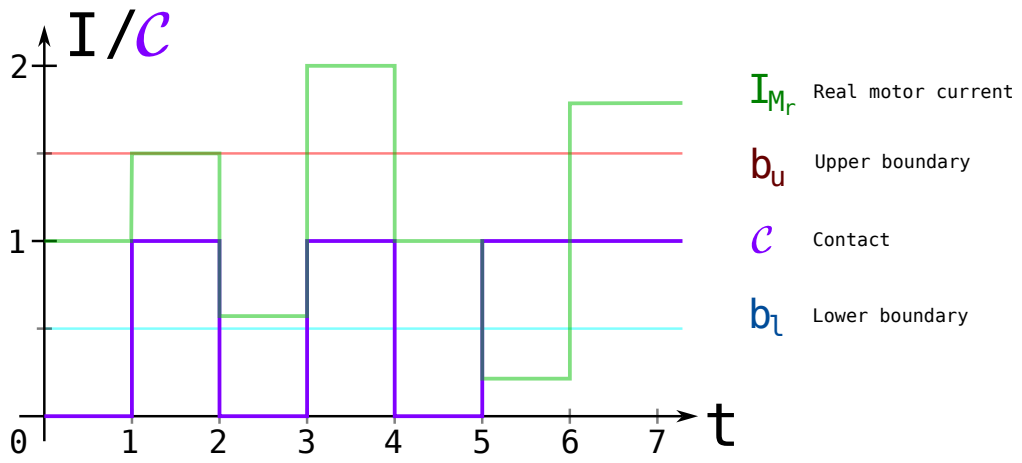

Figure 3.7.: Static-Detection concept.

contact variable $\mathcal{C}$ is assigned the value of zero; otherwise it is assigned the value of one. This process is repeated for each time step t_i, resulting in the detection function

$$\mathcal{C}(t) = \begin{cases} 0 & \text{for } \mathbb{A}_f(t) < \mathbb{A}_c(t), \\ 1 & \text{for } \mathbb{A}_f(t) \geq \mathbb{A}_c(t), \end{cases} \tag{3.33}$$

for $t \in \{t_i \mid i \in \{0, \ldots, n\}\}$.

Remark: This logic can be simplified with constant values for $I_{\mathrm{M_f}}$ and $I_{\mathrm{M_c}}$, that are conducted through real motor current observation for different cases. While constant values are unrealistic for the Calculated-Detection algorithm since it is anticipated that $I_{\mathrm{M_f}}$ and $I_{\mathrm{M_c}}$ vary similarly to the motor current in difference cases, they can still answer to peaks in currents. Setting constant values can, therefore, be a promising approach for initial testing and algorithm development. This simplified concept is depicted in Figure 3.7 and will further be recalled as Static-Detection. Here, no contacts are detected, while the motor current signal, showed in green is inside the boundaries (red and blue). Otherwise, a contact, coloured in purple, is recognised.

3.5. Case Study for Current Estimation

To validate if the estimated motor currents from Equations (3.21), (3.31) are usable in the first place, a central test had to be performed. In detail, this test is described in the appendix under Protocol A. Here five different significant test cases were performed using the current SCOUT platform. Per the test case, three iterations with different durations were taken to ensure that there was no drift over time. This turned out to be the case for the recordings. Most noticeable is that recorded data is very noisy, justifying the use of a filter in order to reliably gather information from the motor current signal. Furthermore, for Protocol A, video recordings were captured, containing footage of the rover while performing these tests. These videos are used to extract estimated contacts. A script developed for this purpose allows the video files to be opened. Manually, for each frame, either zero or one is assigned, resulting in an array that contains information on contacts for a 60 fps video. To map this onto the 100 Hz standard communication of the motor controller, the array is interpolated.

Section 5 includes a discussion of this topic, but first a model verification must be considered. To do this, the mathematical model is programmed and then implemented using a simulation software. The models are then adapted to the onboard application.

4. Model Verification and Validation

This chapter is concerned with the verification of the model, first, regarding an offline post processing program with Python. In this section the programs used for dimension validation and estimating contacts are described. To provide context for the results of these algorithms, this section summarises a simulation developed in Dymola. These then lead to the onboard implementation, which is explained lastly. The description of these programs sets the stage for the following Chapter 5, in which the results of these implementations are visualised and discussed.

4.1. Offline Signal Analysis with Python

Model verification is an important step in development and for that visualising values is beneficial. That is why Python is used as the development programming language. The open-source platform offers free libraries for many topics such as numerical analysis, signal processing and plot visualisation [VRD09]. With Python, a variety of numerical problems can be solved and analysed [Kiu13]. [1]

4.1.1. Dimension Validation

The first program necessitates the package `numpy` for numerical calculations. All the static variables like the time horizon `t=5.0`, the dimensions given from the motor, and gearbox data sheets and the measured values from Protocol B are inserted.
Important functions are defined subsequently, including a function that produces an exampled acceleration. For verification, it is chosen to be a sine function of frequency and

[1] Utilised version of Python is 3.7.4.

amplitude one or alternatively a constant velocity. Through integration and with the initial conditions $\varphi_M(0)$ and $\dot{\varphi_M}(0)$, the functions $\varphi_M(t)$ and $\dot{\varphi_M}(t)$ can be determined. These are needed since the Equations (3.31) and (3.21) both require these functions.
The calculations for the inertia of masses of wheel J_W and then the total inertia of masses J_tot are also realised in functions.
These values can therefore be used to calculate the free wheel torque $M_{\mathrm{des}_f}(t)$ (3.17), but the gravitational torque M_g (3.29), which is also calculated in a separate function, must still be calculated before the contact torque $M_{\mathrm{des}_c}(t)$ (3.30) can be determined. With the presence of these values, the free wheel and contact currents $I_{\mathrm{M}_f}(t)$ (3.21), $I_{\mathrm{M}_c}(t)$ (3.31) can be derived in individual functions.
Lastly, there is a function that produces a semi random course mimicking a real motor current $I_{\mathrm{M}_r}(t)$. For that, it randomly takes values of $I_{\mathrm{M}_f}(t)$ or $I_{\mathrm{M}_c}(t)$ multiplied by a random value between 0 and 1. It then holds this for a minimum of $t_\mathrm{min} = 0.5$ seconds and then selects a random value $t_\mathrm{rand} \in [0, 0.5]$ and adds this value to t_min to get a varying time window t_win. This resembles the unpredictability of the real system.
By implementing the logic described in equation (3.33), the program evaluates contacts. The value of the program lies in proving the working concept of the motor current calculation and the contact detection logic, but has little value for the onboard implementation. The results of this verification can be seen in Chapter 5.

4.1.2. Post-Processing Contact Detection

A Python program has been developed to facilitate the evaluation of recorded data. Utilising the `tkinter` library, easy file browsing and the selection of multiple files is supported, which proves to be highly practical considering the multitude of files generated during the experimental tests outlined in Protocol A. The OBC saves the motor controller data into HDF5 files, which can be accessed retrospect with the `h5py` library. These files contain information on motor currents and angular velocities, amongst other things. The needed data sets are isolated in order to be processed.
The recorded angles φ_W and angular velocities $\dot{\varphi}_W$ are important for subsequent calculations. It is important to note that the internal model, based on Dymola, directly converts into wheel angles. While the data on angular acceleration is not directly provided, it can be derived from the angular velocities. Since discrete time points t_i, $i \in \{1, \ldots, n\}, n \in \mathbb{N}$ are sampled by the motor controller, the change in angular velocity $\Delta\alpha_W(t_i)$ between

consecutive time steps t_i and t_{i+1} allow to compute the angular acceleration $\alpha_W(t_i)$. By dividing $\Delta\alpha_W(t_i)$ by the time step $\Delta t = 0.01$s [Ave20] a discrete acceleration can be derived [OV98], resulting in

$$\Delta\alpha_W(t_i) = \omega_W(t_{i+1}) - \omega_W(t_i) \quad \text{and} \quad \alpha_W(t_i) = \frac{\Delta\alpha_W(t_i)}{\Delta t}. \tag{4.1}$$

Continuing with the available data, the estimated free wheel currents $I_{\mathrm{M}_f}(t)$ and contact currents $I_{\mathrm{M}_c}(t)$ are calculated, allowing for comparison with the real motor current $I_{\mathrm{M}_r}(t)$, extracted from the HDF5 files. The contact detection logic, based on the calculated and real motor currents, is integrated into the program.
The Static-Detection is also incorporated to assess the performance of the implemented Calculated-Detection algorithm. As already indicated in Figure 3.7, the Static-Detection follows a simpler approach. Here, upper and lower boundaries, b_u and b_l, which are manually tuned, based on observations from the experimental tests outlined in Protocol A respectively, are defined. They form a 'tube' in which no contact is assumed, and any deviation outside this tube results in the detection of contact. The Static-Detection algorithm's logic

$$\mathcal{C}(t) = \begin{cases} 0 & \text{for } (I_{\mathrm{M}_r}(t) > b_l) \wedge (I_{\mathrm{M}_r}(t) < b_u), \\ 1 & \text{for } (I_{\mathrm{M}_r}(t) \leq b_l) \vee (I_{\mathrm{M}_r}(t) \geq b_u) \end{cases} \tag{4.2}$$

can be derived for $t \in \{t_i \mid i \in \{0, \ldots, n\}\}$.
Small errors can occur due to zero crossings of the time axis. Therefore, a filter is applied that cancels out narrow contact detections with a non-realistic contact time span. A contact threshold $c_t < t_i - h_t$ is defined that sets the width of non-acceptable detections. This is coupled with a verification time t_v, delaying the correction. This results in a for-loop that first checks if the contact function $\mathcal{C}(t)$ is zero at the interval borders of $[t_i - t_v, t_i - t_v + c_t]$. If so, the for loop continues checking for every time step if $\mathcal{C}(t) = 1$ for any $t \in (t_i - t_v, t_i - t_v + c_t)$. If so, $\mathcal{C}(t)$ is set to zero in the interval. This is done for every time step, filtering out noisy detections. The width of the filter is adjustable with c_t. A schematic of this filter can be seen in Figure 4.1. In purple, the contact function $\mathcal{C}$ is shown, which is one for a time period inside the filter-window. Therefore, this detection would be treated as false detection and would be filtered out accordingly.

The performance of these algorithms, compared with each other, are presented and discussed in Chapter 5.

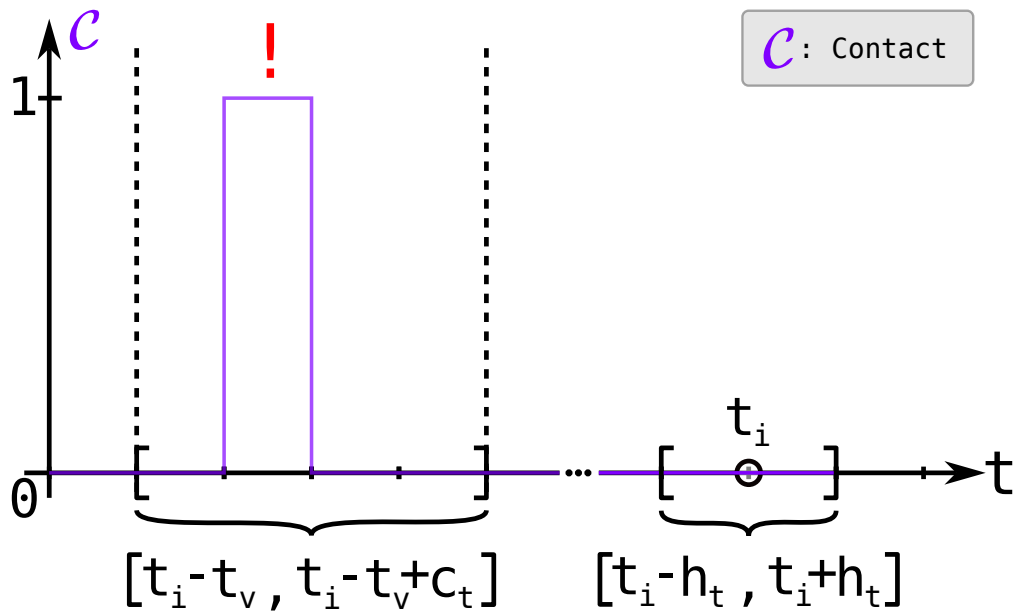

Figure 4.1.: Filtering principle of noisy detection.

4.2. Multibody Model in Dymola

Dymola offers a variety of tools in their in-house libraries. Most of them present basic components, like weights, springs, resistors and bodies. Out of these simple elements, basic structures can hierarchically be defined. Components like motors and wheels can then be crafted into e.g. vehicles or robots. Together with a plot-visualisation, behaviours of the model can be pictured.

In the case of this research an in-house visualisation toolbox is utilised that even allows the user to view complex 3D-models in a simulation. This allows testing of the model's fidelity not only through plots and graphs but also through videos and renders, showing estimated behaviour.

4.2.1. Multibody Model Configurations

The model created in this thesis includes an abstracted Rimless-Wheel model. Beyond that also lies a gearbox and a motor model that are not visualised. They are the offspring of the already created libraries for the SCOUT-Rover [HBB17]. These parts are used to construct a new simulation model, fitting the purpose of detecting motor currents in the wheel. These currents serve to see if the assumptions made in the Equations (3.21) and (3.31) can project the behaviour of the wheel.

In Figure 4.2, the simulation model is shown. In the centre all the components of the drive chain can be seen as in the applied model. In the upper left corner, the terrain generation takes place. Here, a fixed coordinate system "world" is placed at the fixed coordinates [0,0,0]. Then, an elevation map is connected to this coordinate system. Next to it, parameter definition and visualisation is located.

The elevation map is part of the in-house libraries and can be configured with different surfaces, terrains and substrate materials. An options menu for the elevation map leaves the choice open for soil parameters, different grain sizes and contact models [HBB17]. In this case, no stone or gravel is needed, therefore, it is set to be a flat and non elastic substrate condition. Under the surface tab, all the options are listed. For resembling the different cases tested in Protocol A, the "HeightMap" is used, except for the last case, which utilises a random surface that is generated using the "Noise"-surface option. [BPB23]

In the upper right corner of Figure 4.2, the DLR-Watermarks, the simulation time, the parameters of the SCOUT-Rover and the "Visualisation 2" toolbox can be accessed. They did not need to be changed, except for the parameters. These are adjusted according to Section 3.1 and to the weight fraction evaluated in the Protocol B. The simulation time is set to 20 seconds, leaving enough room to evaluate the currents. [BPB23]

The main section of interest is the wheel and motor model. Here, a fixed frame for the coordinate system is inserted, which fixes the wheel in place for the z-coordinate. This connects to two consecutive prismatic blocks that allow the wheel to move along the x-direction and to revolve around the z-axis. The drive-chain model is inserted with a virtual BUS-communication that processes inputs. These inputs are currently set to be

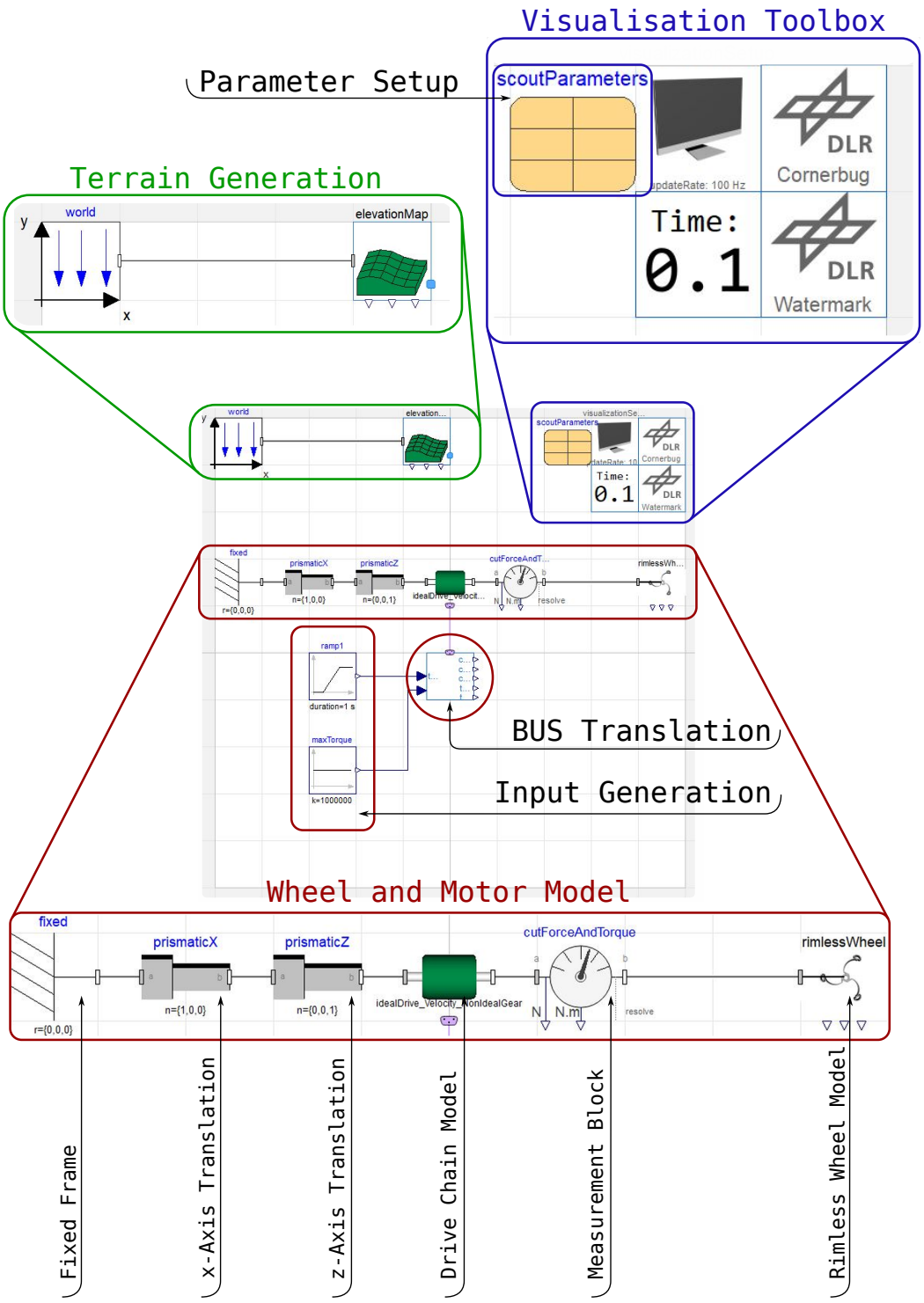

Figure 4.2.: Simulation model in Dymola.

a maximum torque and a velocity. From the velocity and the starting points given in the fixed frame, Dymola calculates all values of interest.

In Figure 4.3, the depth of the hierarchical structure is depicted. A detailed view of the ideal drive can be observed. The components of the gearbox, the motor and the servo drive are depicted. These lowest submodules consist of basic components given in the basic Dymola libraries [HBB17]. This component flows into a cut force and torque sensor, which then subsequently leads into the model of the Rimless-Wheel.

In Figure 4.4, a zoomed-in view on the Rimless-Wheel is presented, also featuring the integration of the spokes, consisting of two straight beams, that are connected at a fixed angle. This could also be modified [HBB17] in an options menu, but considering the assumptions made in 3.1, they are set to be stiff. Also illustrated on the right-hand side is a green block that sources a CAD-file for the specialised feet. It is important to point out that for the simulations used, only the feet collide with the elevation map. Other options could be set, like spoke and feet flexibility and contact dynamics. [BPB23]

4.2.2. Simulation Settings

This model is created to find a compromise between the purely mathematical model and the real system, incorporating the mathematical models' approaches and combining them with the option to simulate different terrains. Furthermore, this simulation offers possible comparisons to compare the test carried out in Protocol A and analogue cases carried out in Dymola. For that, five cases have been chosen to be simulated in Dymola:

1. Wheel is fixed at a constant height and spins freely

2. Wheel can freely move forward on a flat surface

3. Wheel is fixed at height but makes contact with the ground

4. Wheel can not move forward but remains spinning

5. Wheel moves on randomly generated surface

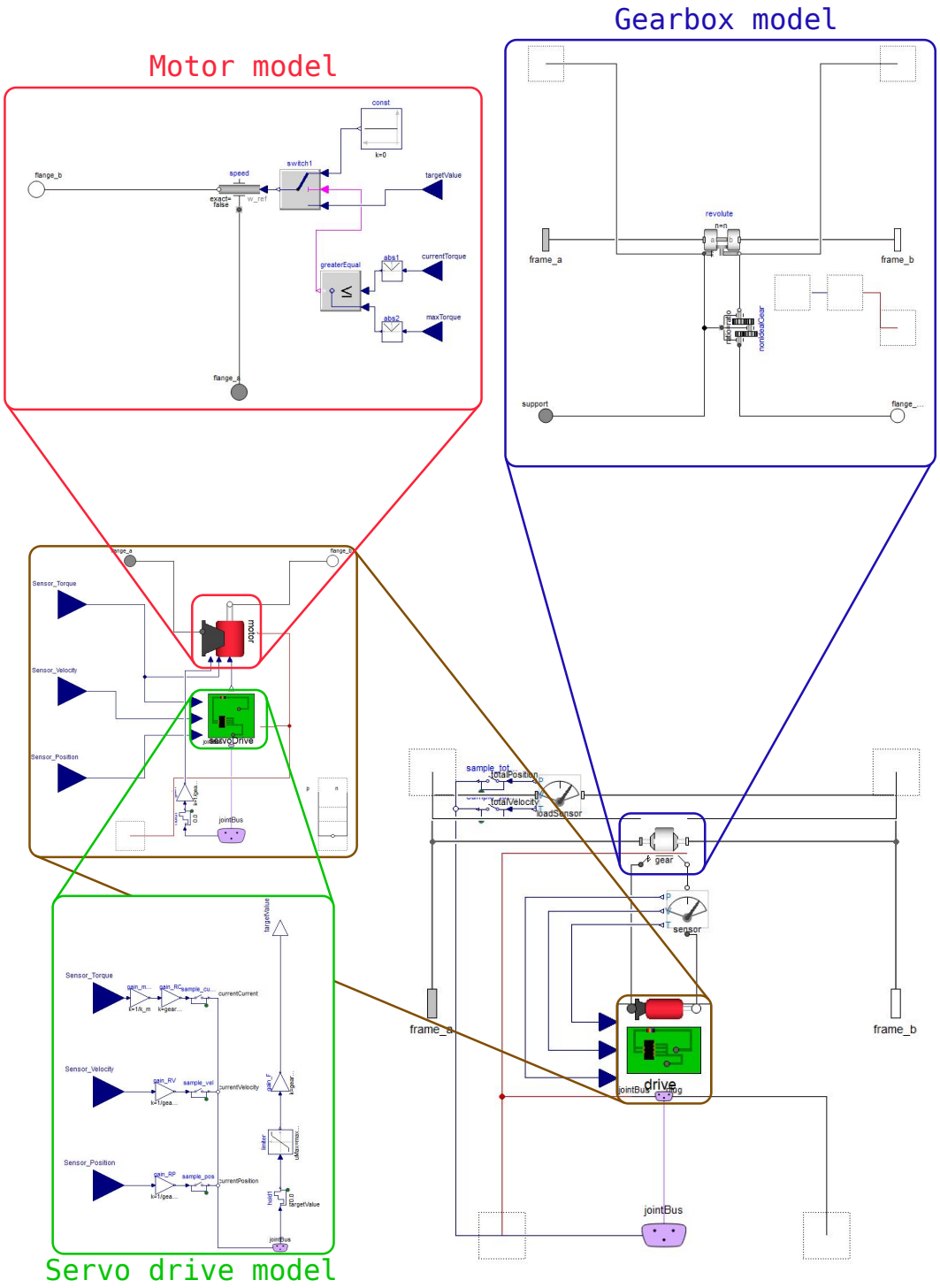

Figure 4.3.: Detailed view on the ideal drive chain in Dymola.

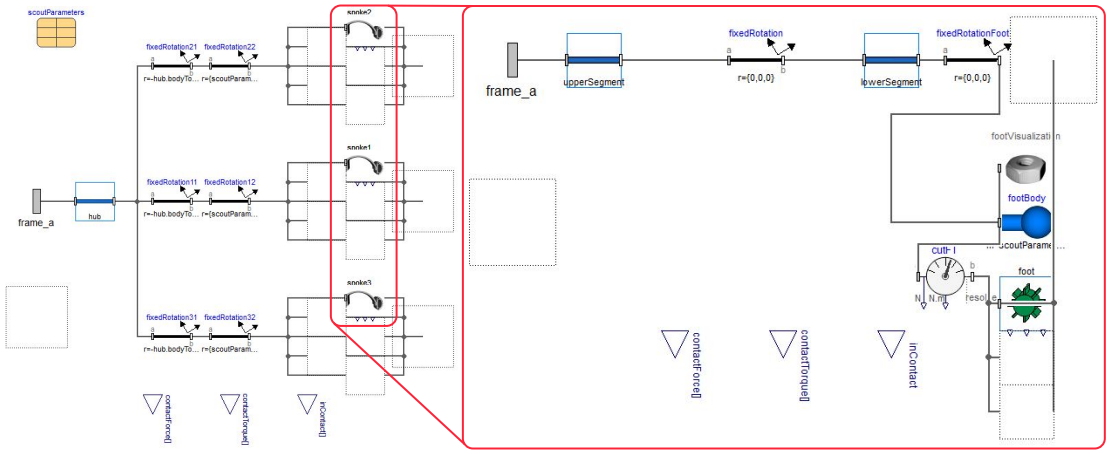

Figure 4.4.: Detailed view on the Rimless-Wheel in Dymola.

The results, also compared to the real motor currents and the calculated motor currents, can be seen in Section 5.

4.3. Online Contact Detection with ROS2

The current SCOUT version performs on a Dymola model [PSLa22]. This requires a lot of calculation power that could be used more efficiently. The Robot Operating System or short ROS2 offers a possible solution. Compatible with communication on the EtherCAT standard, this open-source middleware offers a fast and efficient communication between the onboard computer and the components of the SCOUT-Rover.

ROS2 is structured in publisher and subscriber nodes. A publisher publishes so-called topics, that can be subscribed from multiple subscribers. Based on this simple concept, complex communication systems can be created. [MKA16]
With the application `rqt`, various visualisations can be made, such as communication diagrams that visualise subscribers and publishers and the nodes in between, which can be seen in Figure 4.5. Beyond that, graphs can be shown. The results are shown and discussed in the Chapter 5.

The new SCOUT Prototype is still to be developed. Implementing an onboard contact detection for this communication standard is future-orientated, and the applied performance is therefore not observable.
Nevertheless, verifying a working implementation is crucial. Therefore, a rudimentary publisher and subscriber program are written to simulate data transmission, verifying the functionality of central contact detection. This is conducted on the ROS2-Python language.

4.3.1. Test Publisher

Various information, like motor currents, angles, and velocities, must be collected and published centrally for every motor. This is done to reduce communication latency. To do that, the new message type, `elmo_topic`, is defined. This name refers to the motor controllers that will be used in the upcoming prototype. This message type is hierarchically structured and includes all the information the later prototype needs. The test publisher publishes under this message type. The program publishes values extracted from the same HDF5 files that were recorded during the tests presented in Protocol A, with a frequency of approximately 100 Hz.

4.3.2. Onboard Contact Detection

The topic published by the test publisher is subscribed by the onboard contact detection. The required data is then extracted from the hierarchical communication structure and filtered using a Savitzky-Golay filter. This lowpass-filter is known to perform well and fast. It is based on polynomial regression, and parameters can be set and tuned manually

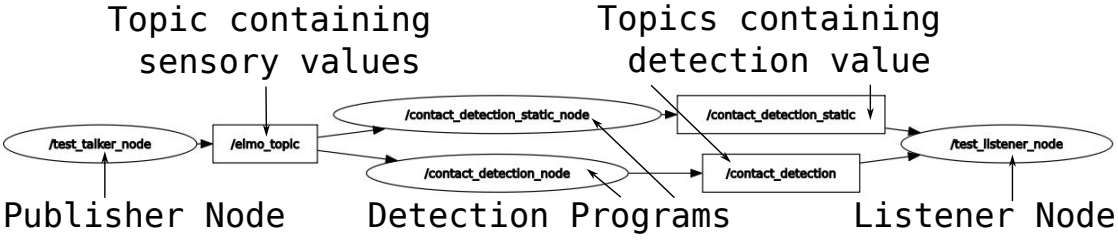

Figure 4.5.: Node and topic structure of ROS2.

[KS12]. Through testing, a polynomial order of 4 and a window size of 51 was evaluated with the Python program of 4.1 to be acceptable. This relatively big window size is necessary since the noise amplitudes can reach up to 200 mA, making an unfiltered contact detection under this approach unusable. This means the algorithm requires a certain start-up time, and therefore, has a time delay. However, this is still quite small and can be significantly improved if the future system works with a higher sampling frequency later.

The core function of the central contact detection remains similar and offers two versions. One with that features the Calculated-Detection and an other featuring the Static-Detection, providing the future prototype the choice between two algorithms. The changes required to run the code on ROS2 are mainly related to notation and the distribution of data reception at specific time points. This includes a time window selection being as large as the window size of the filter. This means that only necessary data is saved, improving the performance and data consumption of the algorithms.

The two detection programs then publish recognised contacts under a central topic called `contact_detection_status`, with a slight time delay. It consists of the calculation time and the filtering delay. As described in Figure 4.1, the principle of filtering noisy detection is also carried out. Here, the verification time t_v lies within the boundaries of the time window to avoid further delays.

4.3.3. Test Listener

Once the data is processed in the central detection programs, the subscriber subscribes to the `contact_detection_status` topic and then prints its results to the console. This topic only transfers boolean values and is designed to handle all motor values at once. This program initially completes the communication network for this ROS2 application. However, it is to be expected that this structure will be much more complex in the real prototype, and that only the central contact detection algorithms will be integrated. In this context, the test programs are only verifying components, and the next Chapter 5 deals, amongst other things, with the results generated with this simplified representation.

5. Results

Various models are explained in Chapter 3 and the last Chapter 4 concludes the theoretical methods for contact detection. Visualising these methods enables profound comparisons and also highlights difficulties, promoting a deeper understanding of the outcome of this thesis. The different tools, such as Python, Dymola and ROS2, are used to visualise the results of the theoretical approaches, which are compared and discussed in this chapter.

5.1. Offline Signal Analysis with Python

This section features the results of the programs described in Section 4.1. For visualisation, the Python library `matplotlib.pyplot` is used, handling plots and their vividness.

Figure 5.1 shows the results of the different torques that are derived in Section 3.2.2. On the left side in Figure 5.1a coloured in blue, the gravitational torque function is shown when inputted a constant angular velocity shown in green. In periods of $\frac{2\pi}{3} \mathrel{\hat{=}} 120°$ the torque starts at its maximum, resembling the initialisation of lifting the rover and an eminent contact. At $\pi \mathrel{\hat{=}} 180°$ the wheel stands upright on one foot, reaching its highest point. The wheel acts like an inverse pendulum, with the highest potential energy at this point. If the wheel continues to rotate, it will fall over and return its energy to the system, resulting in a negative torque value. When the wheel approaches integer multiples $\frac{2\pi n}{3} \mathrel{\hat{=}} 120°n$, the cycle continues. Since $\omega_W = 2\,\frac{\text{rad}}{\text{s}}$, the period duration is exactly π seconds long.
A different angular velocity can be observed on the right-hand side in Figure 5.1b. The according acceleration, velocity and position can be seen in the lower plot. The

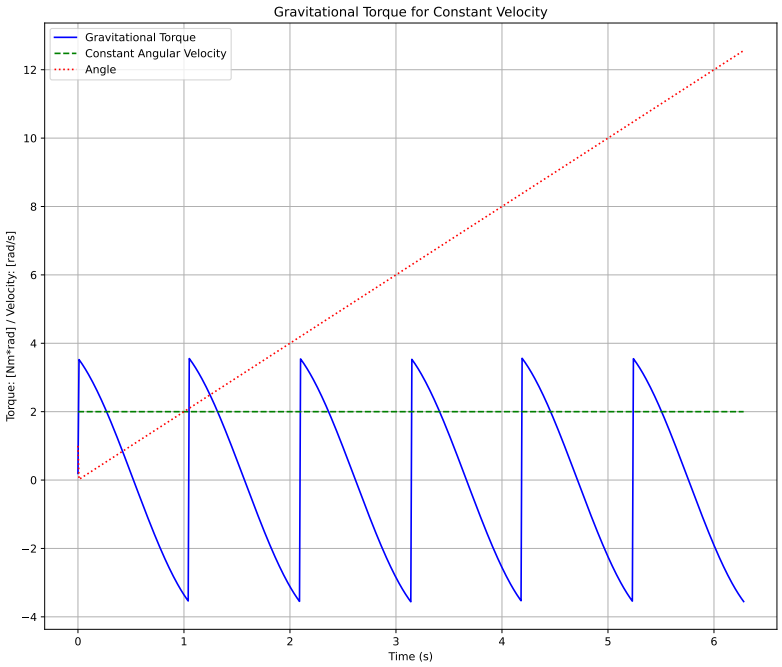

(a) Course of gravitational torque for a constant angular velocity.

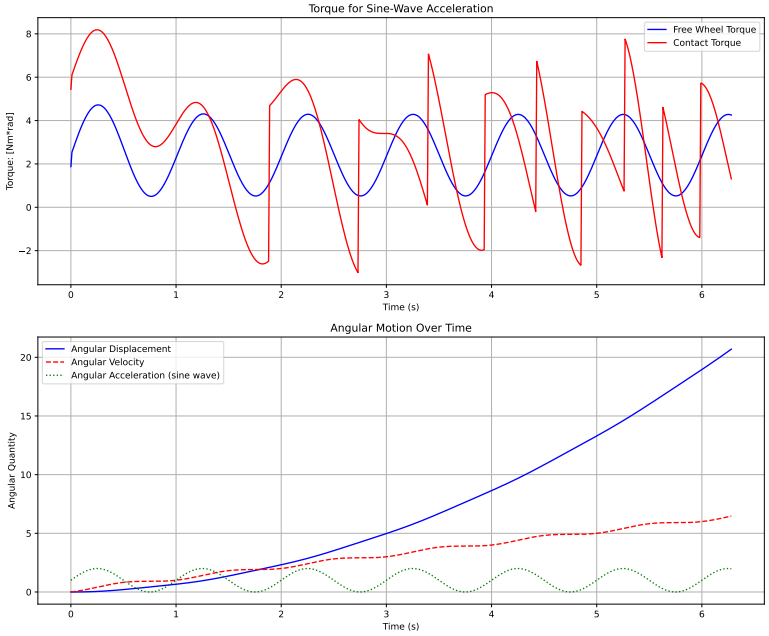

(b) Free wheel and contact torque for a sine-like acceleration.

Figure 5.1.: Behaviour of torques for different angular accelerations and velocities.

calculated free wheel (blue) and contact torques (red) can be examined in the upper plot. As expected, the free wheel torque, coloured in blue, is rather smooth, following the same frequency as the angular acceleration. The contact torque is different from that since the influence of the gravitational torque is present, making the peaks more significant, as it would be expected from the real system.

In Figure 5.2a, the difference between the torques and currents is made apparent. The currents appear much smaller than the torques which is expected since the SCOUT is set to operate with currents lower than three ampere. For the exemplary case with a sine-like acceleration, no significant spikes are expected as well. The observation makes it clear that the conversion is sensible and that values lie within a reasonable value range. This leads to the conclusion that the mathematical modelling is successful for simple cases and that the model is promising for further consideration.

In Figure 5.2b, a randomly generated motor current signal as described in Section 4.1 can be seen. It resembles a real motor current on which the two different contact detection algorithms can be tested and evaluated. Note that this random signal has no correct answer to a contact since no real contact ever happened. It serves the purpose of evaluating the working principle of the detection algorithms.
The performance of these principles, which are outlined in Section 3.4, is depicted in Figure 5.3. The upper plot shows the contact, shown in purple for the Static-Detection. The functionality of the detection tube is made vivid. When the simulated motor current is above or under a certain threshold, the algorithm returns $\mathcal{C} = 1$ for this time step. Otherwise, if the value is inside of these borders, it remains zero. With information on the real contacts and respect to the cases, these thresholds can be tuned to minimise the error.
The lower plot of Figure 5.3 shows the behaviour for the Calculated-Detection. When comparing the two graphs, it is important to note that they can produce significantly different results. This shows that the individual algorithms produce expected results and can, therefore, be used to analyse recorded data from SCOUT-Rover tests.

The values that are saved into the HDF5 files have clear curves, but noise is just as clearly recognisable. To be able to make precise statements, the signal must be filtered. As stated in Chapter 4, a Savitzky-Golay filter is used for that. Figure 5.4 shows the filtered motor current signal for case 1.1. The highlighted magenta curve shows the filtered signal, with the original data in the background, displayed in pink.

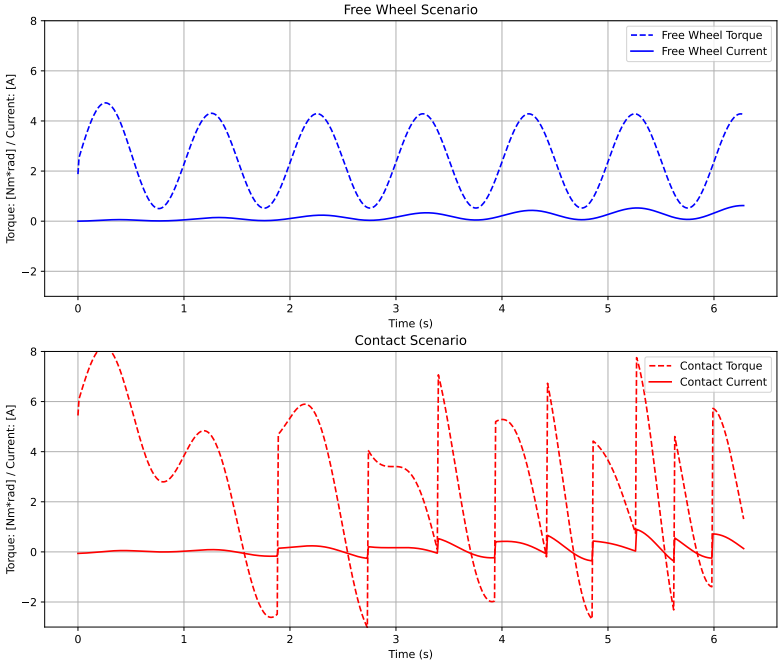

(a) Torque and current compared for free wheel and contact cases.

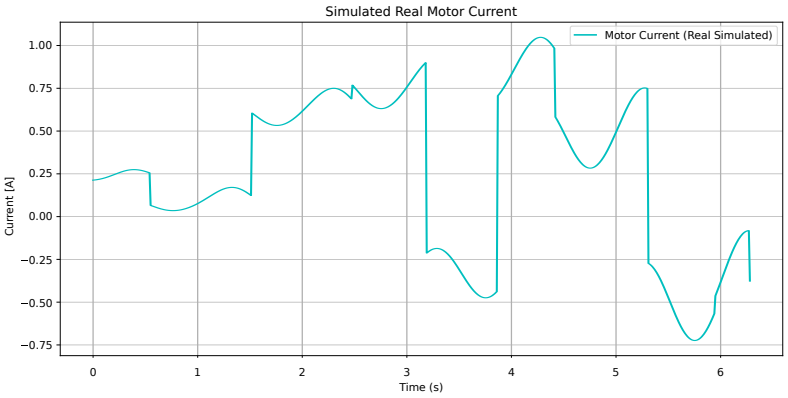

(b) Randomly generated motor current signal.

Figure 5.2.: Motor current generation.

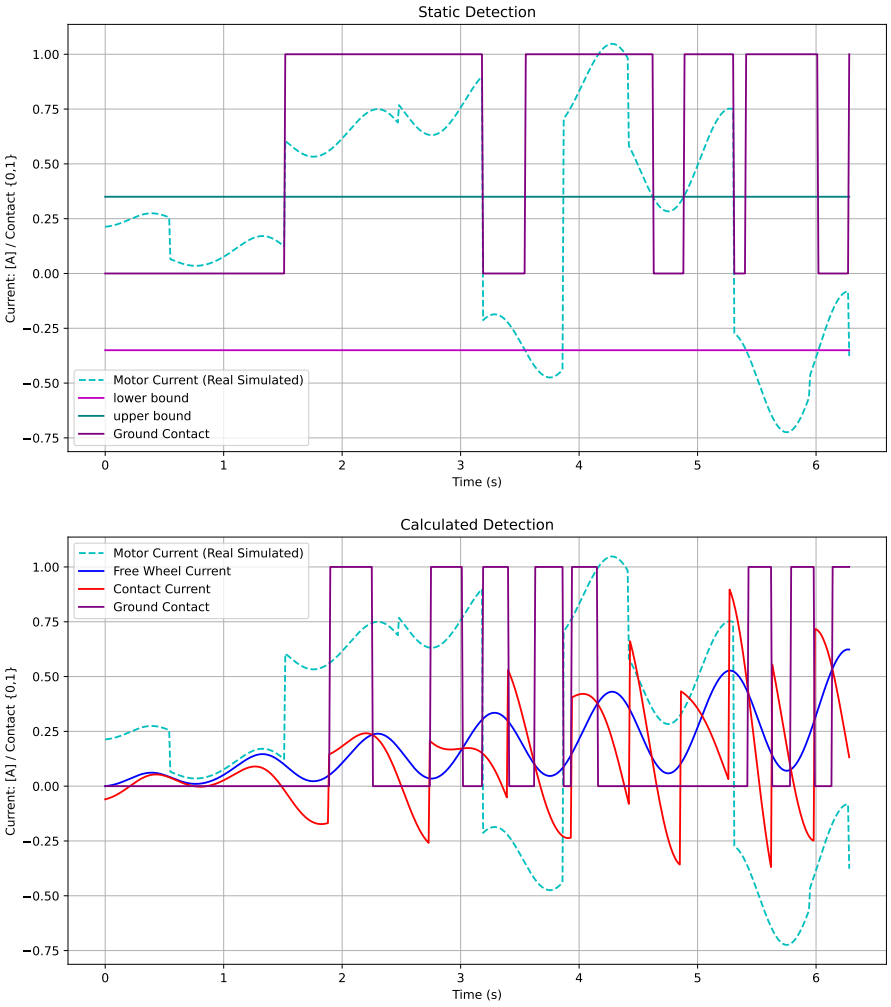

Figure 5.3.: Static and calculated detection on simulated motor current.

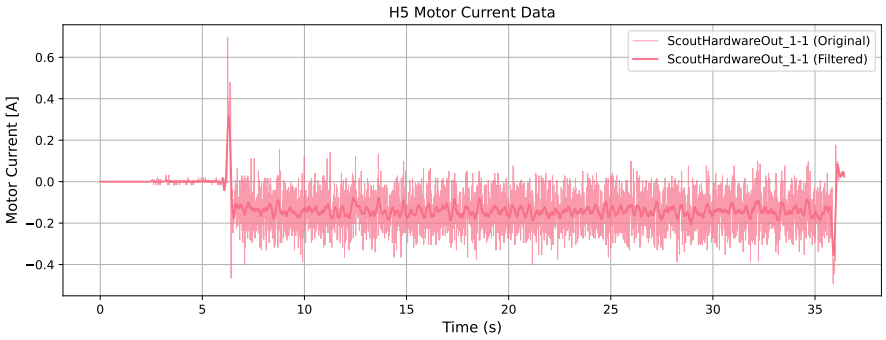

Figure 5.4.: Filtered motor currents for case 1.1.

This figure proves that the noise is striking for the currents, with amplitudes of up to 200 mA, justifying the usage of a filter.

As accelerations are not calculated internally during data transmission, it is crucial to calculate them as they are required in the torque calculations of (3.17) and (3.30). Equation (4.1) describes how to calculate these angular accelerations for this discrete case. The results of this calculation, along with the corresponding angular velocities (dotted), are shown in Figure 5.5.

In the tests of Protocol A found in the appendix, the analysed values are recorded. Videos were also recorded for further verification. For the evaluation of these videos, an approximate real wheel contact was analysed for every frame. This was carried out for all recordings and each motor. Exemplary results are plotted for cases 1.1, 3.1 and 4.1 and continue to be of interest. They can be examined in Figure 5.6 [1]. The results of cases 1.1 and 3.1 are not surprising since the aim of these tests was to either have no contact with the ground at all or to have constant ground contact. This results in constant values seen in Figure 5.6a and Figure 5.6b. Case 4.1 is more interesting since the wheel is connected to the ground in the first part of the recording, but the motors were not powered. This makes the contact unobservable for the motor currents. Once the motor starts, it still has contact with the ground, but the duration is not shown. This results in 7 distinct ground contacts over the course of this test.

This concludes and proves the functionality of every component needed to analyse the results of the two central contact detection approaches.

[1] These plots were manually adjusted for readability

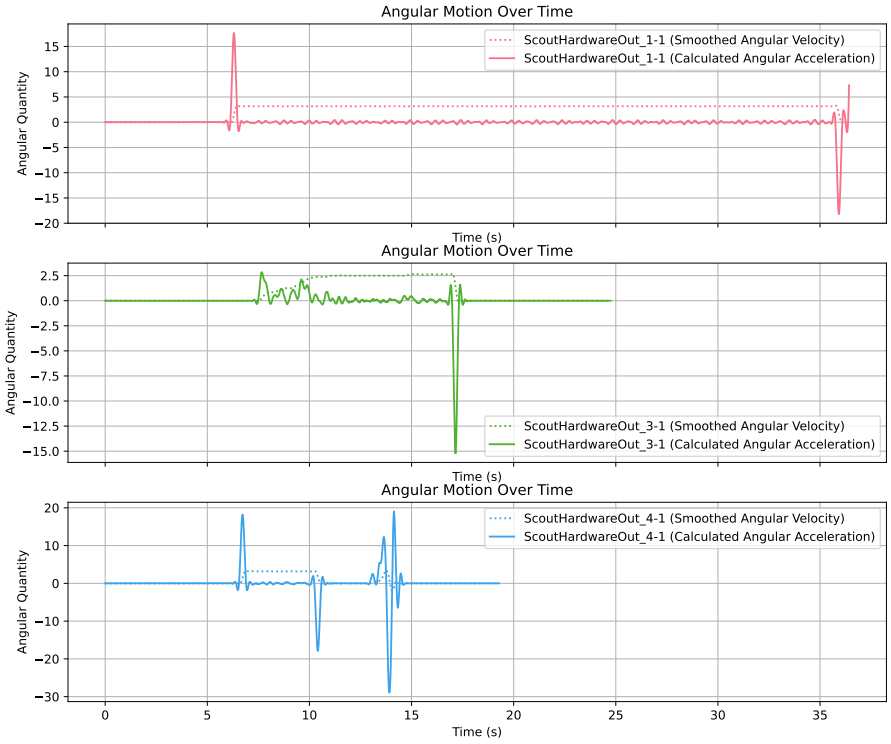

Figure 5.5.: Filtered calculated acceleration for every case.

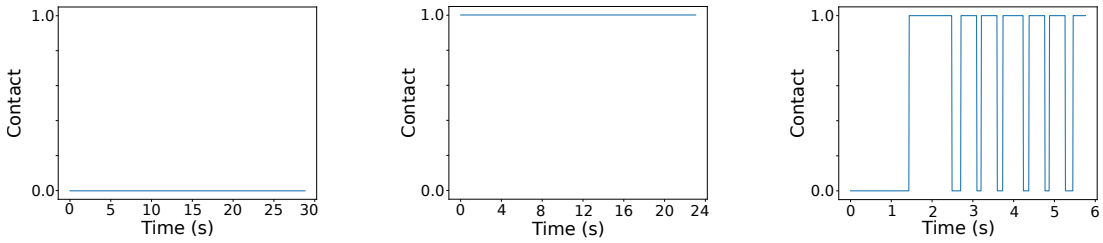

(a) Contacts case 1.1. (b) Contacts case 3.1. (c) Contacts case 4.1.

Figure 5.6.: Contacts for every case extracted from video footage.

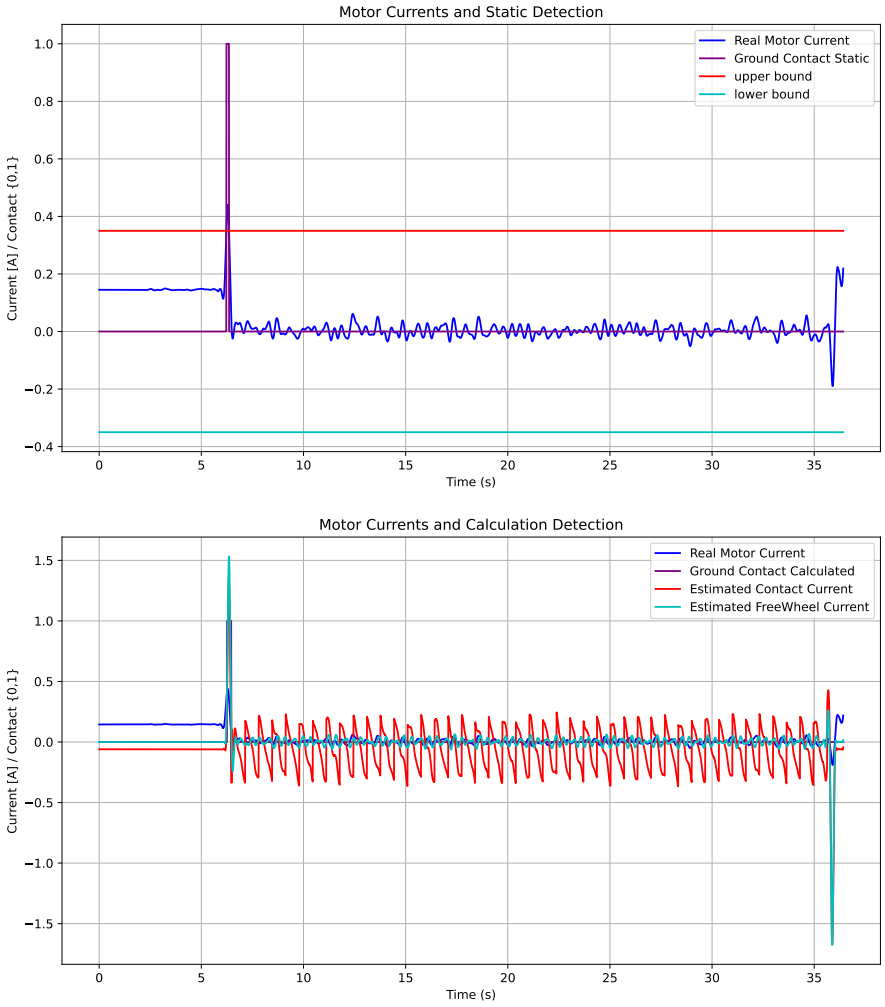

Figure 5.7.: Static and calculated contact detection compared for case 1.1.

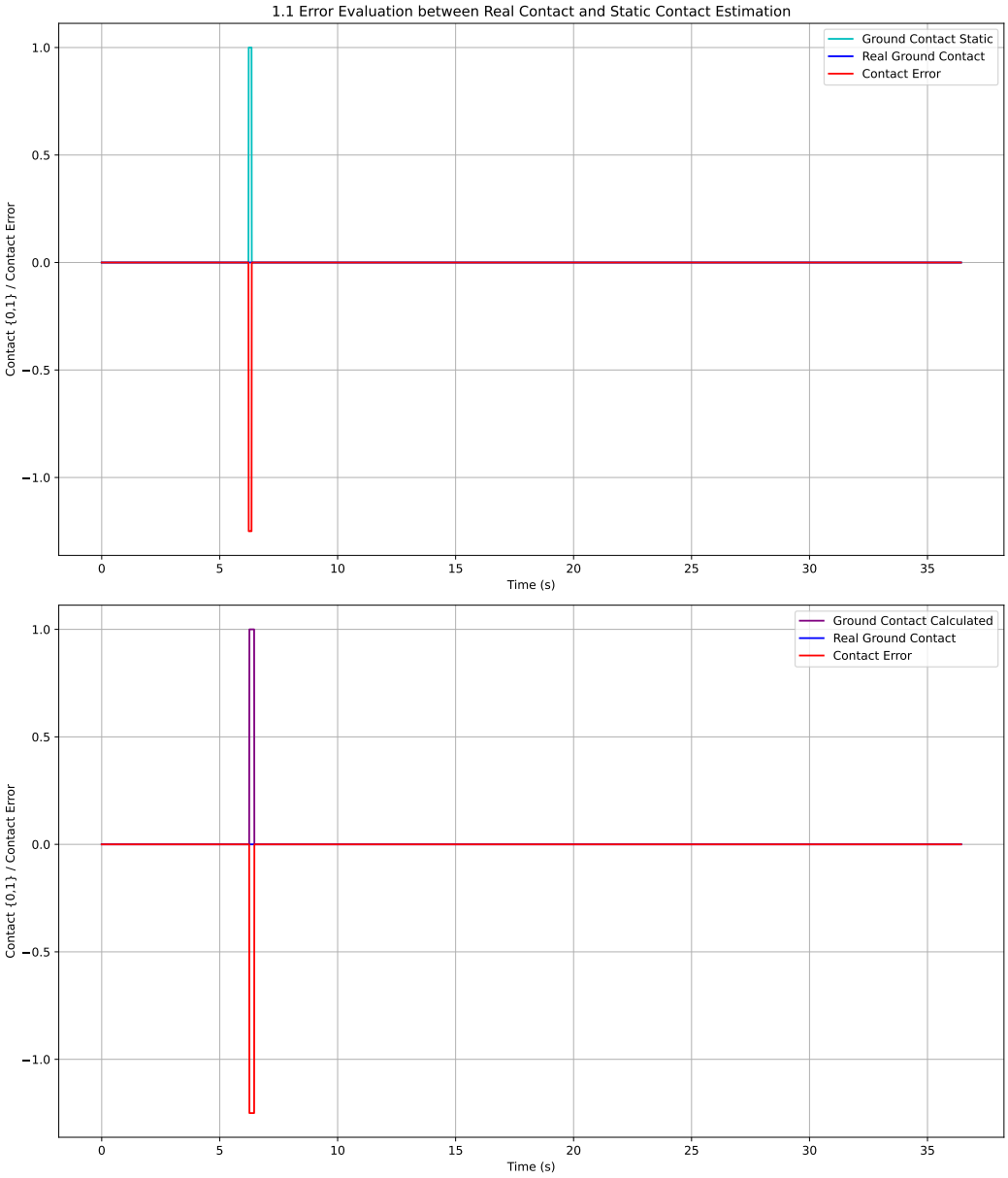

Figure 5.8.: Error visualisation for case 1.1.

In Figure 5.7, the performance of the contact detection for case 1.1 can be observed. The upper plot features the Static-Detection and the corresponding motor current. The lower plot features Calculated-Detection and also shows the corresponding estimated currents as well as the real motor current. It is clear that both approaches detect a contact for an initialisation spike.
To see which approach performs better, every case is compared to the real contacts shown in Figure 5.6. Overlaying these with the calculated currents shows that both have an error, shown in red, for the initialisation, which is depicted in Figure 5.8. In further operation, both approaches behave as expected, as the error remains zero.

Figure 5.9 features plots giving insight into the contact detection for case 3.1. Here, a result of constant ground contact is expected. Both Algorithms detect contact for a majority of the time, but the static approach also detects non-contacts. The calculated approach, on the other hand only has very short non-contact detections. These emerge due to the zeros of the functions.

The errors for case 3.1 shown in Figure 5.10 also reveal that the errors for the calculated contact detection are visibly smaller while driving. The errors on the sides appear significant, but only because, in the video analysis, the contact to the ground is always present, and the motors only register a current when activated. Therefore, the calculated algorithm can only detect the contacts, when the motors are active, resulting in these errors.

In Figure 5.11, the errors for the contact detections for case 4.1 are shown. At first glance it can again be concluded, that the Calculated-Detection has less and smaller errors. However, the error for this case is by far the largest, which is expected, since this case is the most complex. The error for the Static-Detection could be minimised with further filtering, similar to the Calculated-Detection, which filters out unfeasible detections and also parameter tuning, making it a promising approach, even if the errors seem large here.

Valuable data can be taken from the tripod wheel mode, recorded in case 4.1. This scenario is depicted in Figure 5.12. Here, the contact detections for the Static-Detection and the Calculated-Detection can be seen. In this case, periodic non contacts are expected over the operation time of approximately 7 seconds. In Figure 5.6 on the right-hand side seven distinct contacts can be counted while in operation mode. This matches

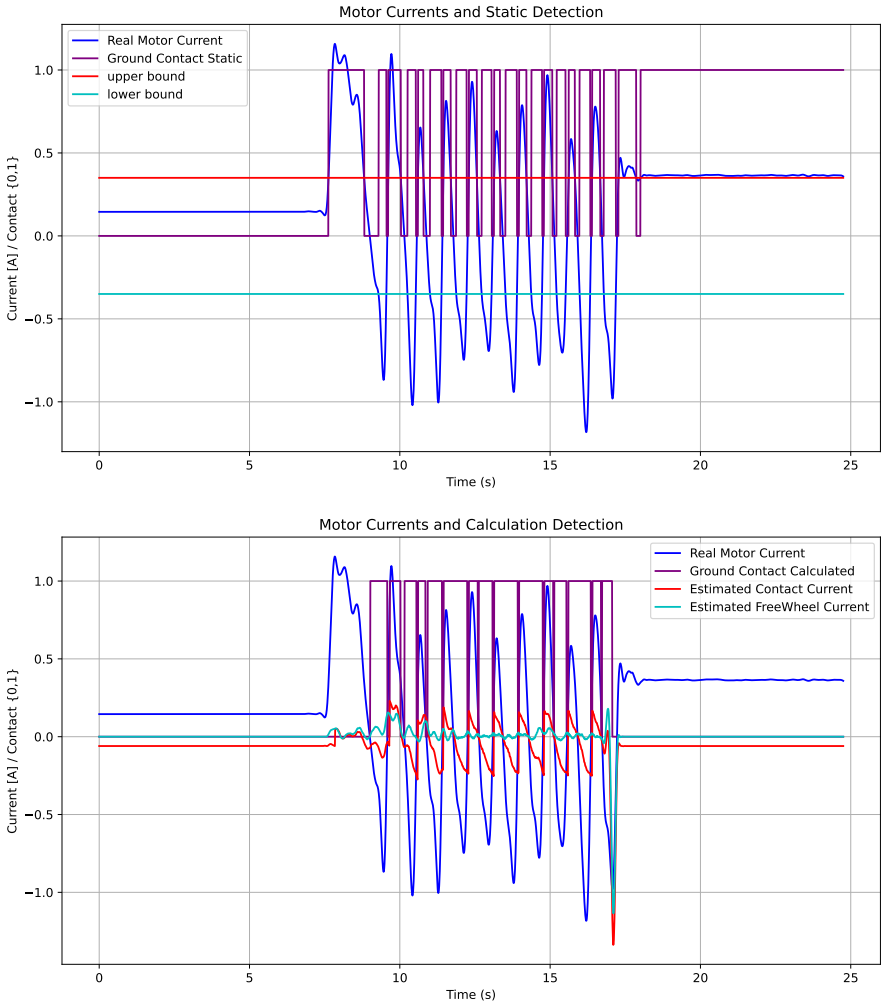

Figure 5.9.: Static and calculated contact detection compared for case 3.1.

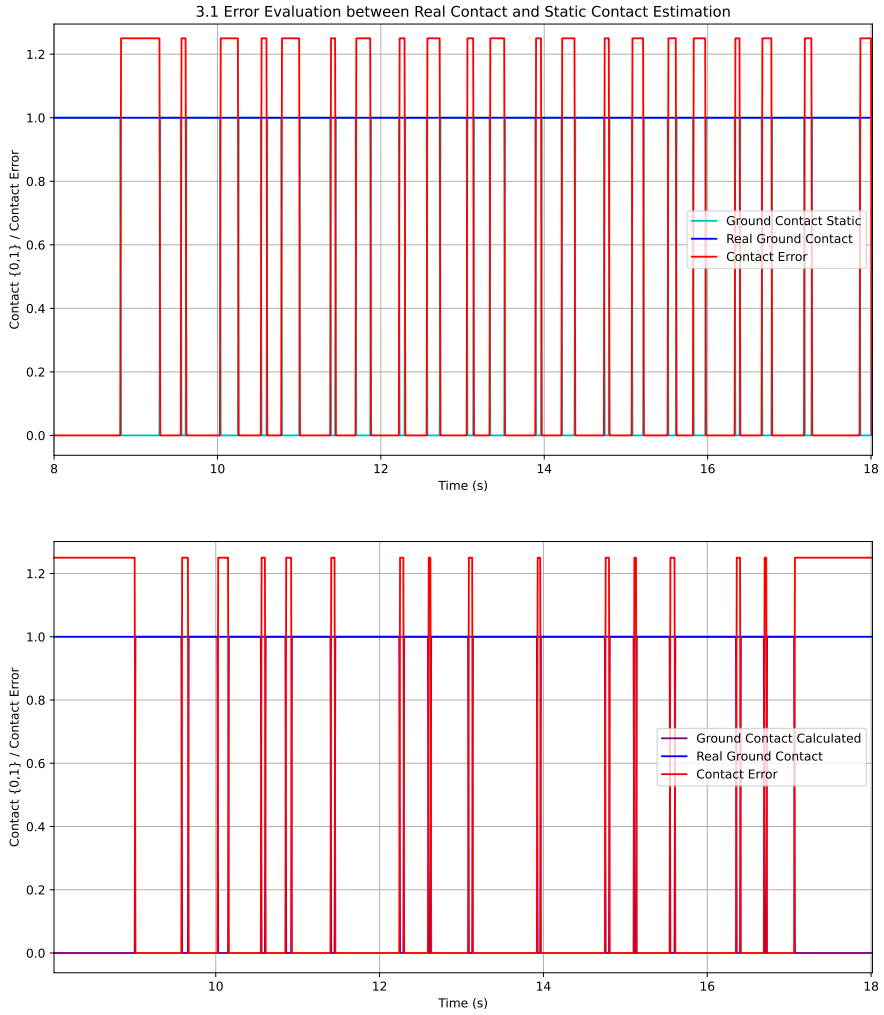

Figure 5.10.: Error visualisation for case 3.1.

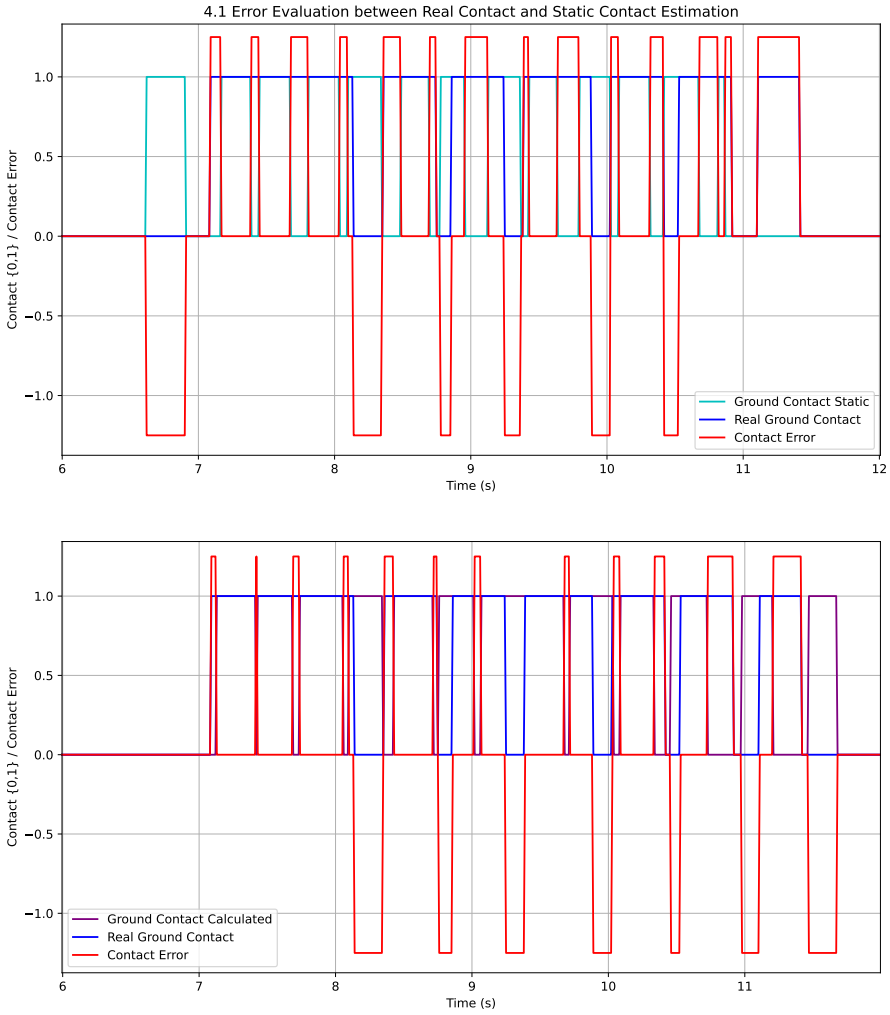

Figure 5.11.: Error visualisation for case 4.1.

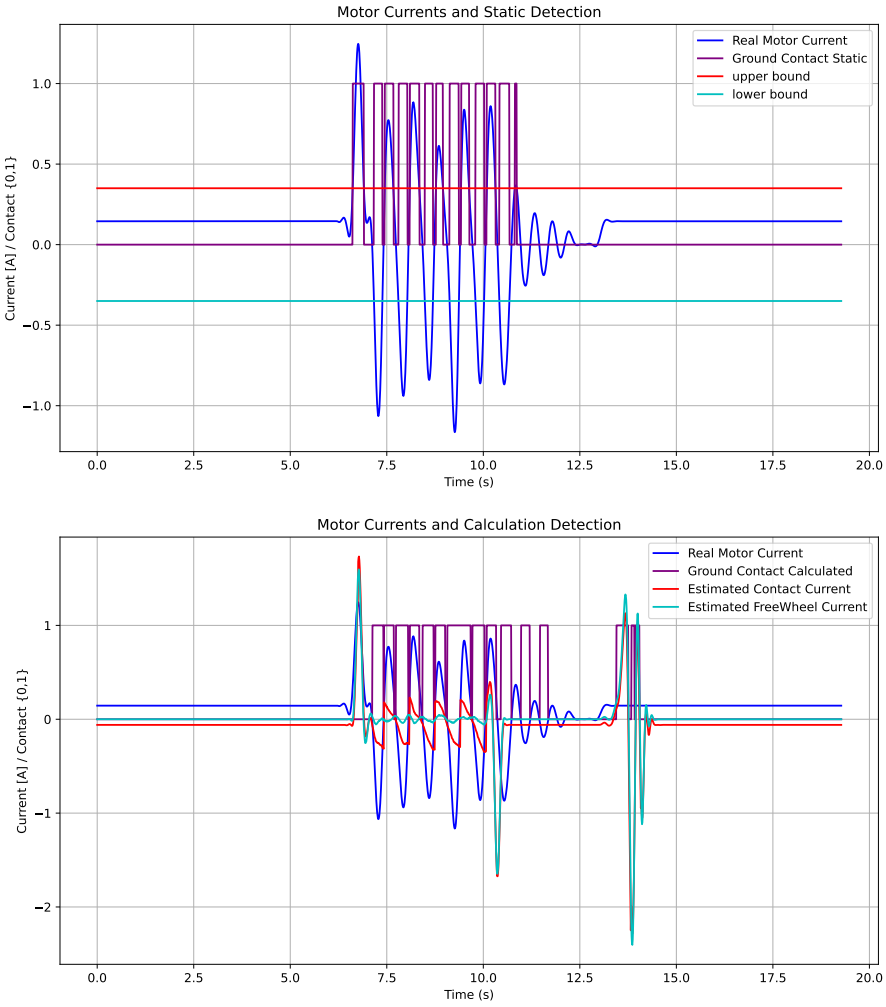

Figure 5.12.: Static and calculated contact detection compared for case 4.1.

the behaviour of the Static-Detection. There are small non-contact detections between apparent detections, which is also likely due to zeros of the function. Similarly, the Calculated-Detection also has this error, and smaller visible contact gaps can be observed. Seven contacts are also recognised when overseeing these errors.

5.2. Multibody Model in Dymola

The results of the calculated motor currents, as shown in Figure 5.1a, are the result of a mathematical model. To test its validity, it makes sense to use a comparative model. As mentioned in Chapter 2, an existing SCOUT model is used to evaluate the rovers capabilities. Therefore, parts of this model were rebuilt to compare motor currents of the simulation with the mathematical model.

The simulation model carried out in Section 4.2 holds valuable information about the behaviour of the motor currents. Similar cases are incorporated into the Dymola model to compare to the mathematical model. Renders of these cases can be seen in Figure 5.13. Here, frames taken from the visual simulation can be observed.
On the left-hand side for the first case, the wheel is fixed in its z-coordinate at a height, where the feet cannot interact with the soil, making it spin freely in the air.
In the centre-left, the second case features a wheel that can progress freely on flat ground. Therefore, it is expected that the wheel always as contact with the ground.
The third case, which is depicted in the centre right, simulates a wheel which is also fixed to a z-coordinate but low enough for the wheel to touch the ground, simulating the motor currents for the tripod wheel mode.
The fourth case, framed on the right-hand side, shows a crevice where the wheel is trapped. It can move freely in the z-direction but can no longer move in the x-direction due to the surrounding barriers. This case is intended to simulate the behaviour of a clamping case. The last case is shown in Figure 5.15a. Here, the wheel has the same freedom as case two but now traverses a randomly generated terrain.

In Figure 5.14, the simulated motor currents for case one and two are shown. It is clear that also, for the simulation model, an initialisation spike can be recognised, as seen in the real motor currents. Compared to them they have no offset afterwards and do not oscillate, remaining constantly zero.

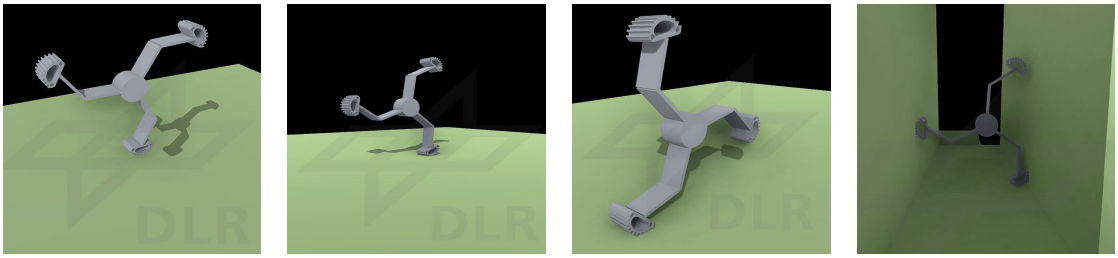

Figure 5.13.: Frames of simulation cases.

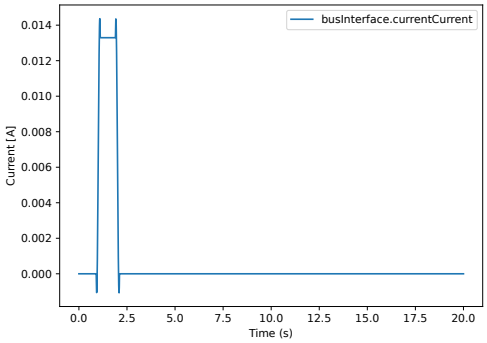

(a) Currents for a wheel spinning freely in the air.

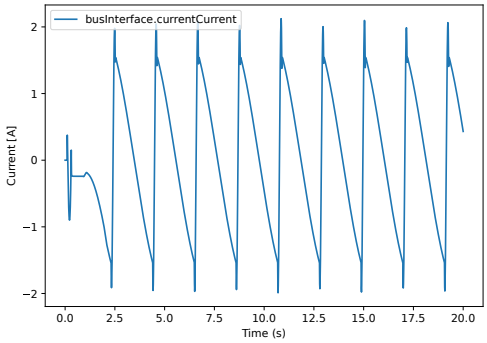

(b) Currents for a wheel driving freely on a flat surface.

Figure 5.14.: Currents for free movement, resembling case 1.1 and case 3.1.

Case two, conversely, clearly features the expected behaviour of a constant contact. The signal has the same qualitative curve as the calculated motor torques, which can be observed in Figure 5.1a for a constant angular velocity, proving the validity of the mathematical modelling.

Figure 5.15b shows the behaviour of the motor currents on a non-smooth surface. It can be seen that both the amplitudes and the phases show slight differences compared to Figure 5.14b.

The exceptional cases represented by cases three and four are shown in Figure 5.16. The tripod gait simulation can be seen on the left-hand side. These curves are different from those for normal unrestricted driving. However, the periodicity is the same, and it is also clear that the motor currents are shortly zero in between. This simulation, therefore, represents a mixed case of cases one and two. The Calculated-Detection is designed based on this realisation and, as seen before, can also handle this case.

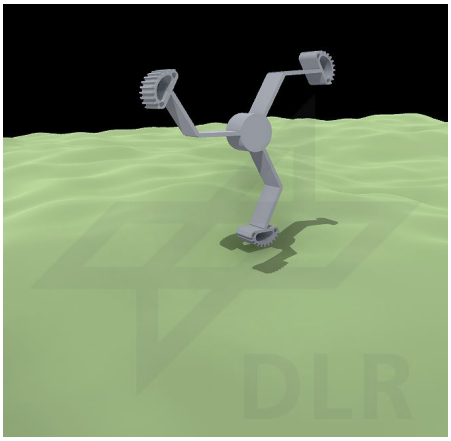

(a) Wheel simulated on randomly generated terrain.

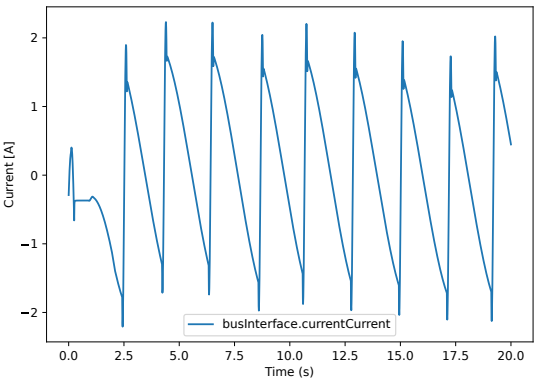

(b) Currents for a wheel moving freely on random terrain.

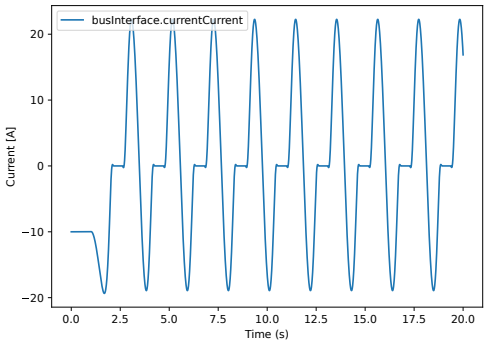

(a) Currents for a wheel fixed in its z-coordinate.

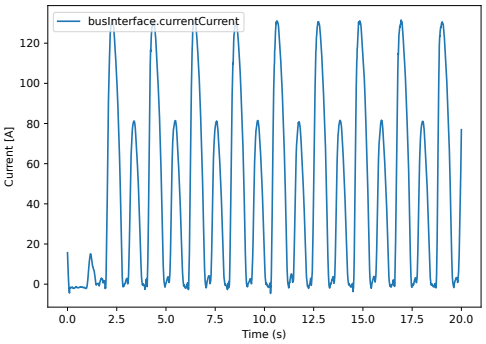

(b) Currents for a wheel trapped in one position.

Figure 5.16.: Currents for restricted movement, resembling case 4.1 and case 2.1.

Comparing the real motor currents and the simulated ones, it is clear that they do not align fully since the real system is inert. In reality, flexible components result in thinning the estimated non-contact time window.

Looking at the results of the simulation, it is reasonable to assume that the mathematical modelling was successful and that the correspondingly good results from the previous observations are not accidental.

5.3. Online Contact Detection with ROS2

Since the mathematical model could be verified by the Dymola simulation, this section now shows how this model performs as an onboard implementation. In Figure 4.5, the communication structure of ROS2 is illustrated, visualised with the plugin `RQT-Graph`. The central communication topic, called `elmo_topic`, contains sensory information on different layers, transmitting an internal clock and transferring data at 100 Hz to the according time stamp. These are then subscribed by the central detection programs that internally filter and evaluate the data, publishing a boolean value under the `contact_detection_status` topic. These are then saved and printed in the listener node `test_listener`.
The individual parts need extensive testing to ensure that the onboard application works on the ROS2 platform. The following Figures 5.17 [2] show the contact detections being executed via ROS2. The same test data from Protocol A is inserted and outputted. The contact histories are clearly similar to those of the original Python program. Notably, initialisation and turn-off errors persist and the static detection remains to appear less reliable.

For case 1.1, seen in Figure 5.17a and 5.17b, the static detection seems superior as only one faulty contact is detected. Here, tuning the noisy detection filter, described in Section 4.1, could have an positive impact on the quality. Since the detections for the Calculated-Detection are smaller than the time window, it can be assumed that the detections are due to data loss in the transmission.
Case 3.1, which is shown in Figure 5.17c and 5.17d, proves the superiority of the Calculated-Detection, having only small errors, while the static detection has very clear non-detections. Notably, this was not the case for the post-processing and could be traced back to data loss in transfer.
In Case 4.1, presented in Figure 5.17e and 5.17f, the Calculated-Detection remains better. Small non-contact phases are visible and the non-contact phases are too long.

[2] These plots were manually adjusted and rescaled for readability

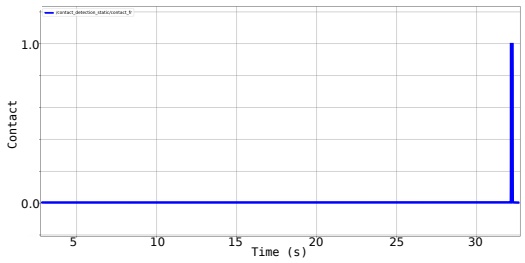

(a) Contacts for case 1.1 for ROS2 static contact detection.

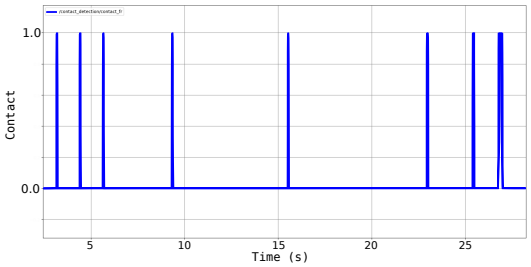

(b) Contacts for case 1.1 for ROS2 calculated contact detection.

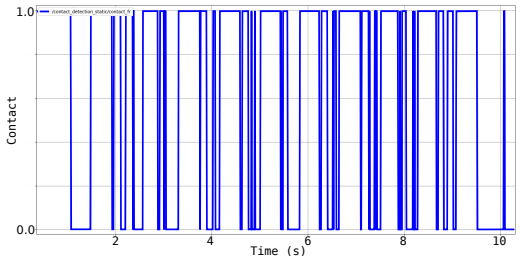

(c) Contacts for case 3.1 for ROS2 static contact detection.

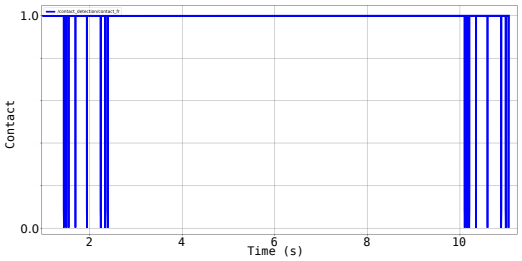

(d) Contacts for case 3.1 for ROS2 calculated contact detection.

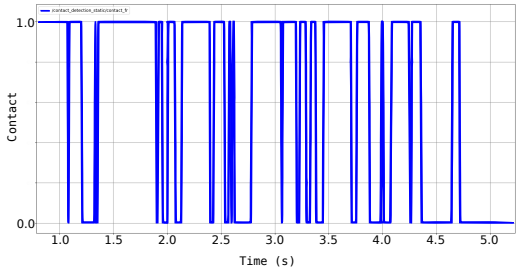

(e) Contacts for case 4.1 for ROS2 static contact detection.

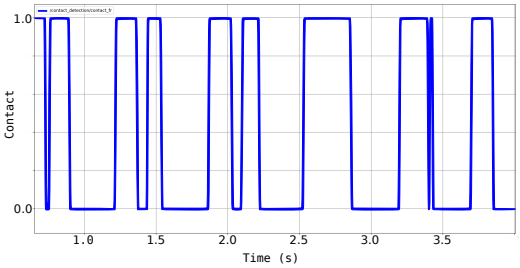

(f) Contacts for case 4.1 for ROS2 calculated contact detection.

Figure 5.17.: ROS2 contact detection algorithms compared for cases.

6. Outlook

The new prototype of the SCOUT-Rover is still to be developed fully, but once operational, the rover can use the developed contact detection right away. The future task for this project will be to integrate the derived contact detection algorithms into the new prototype of the SCOUT-Rover and to test and select the appropriate detection algorithm for it. Other signals can also be used to refine the result of the contact detection, such as the `DriveTarget` signal, which gives information on movement commands or the IMUs for phase shift prevention. Furthermore, this opens up far-reaching possibilities for utilising contact recognition in control algorithms, which also still need to be developed. This represents the final result of the thesis. However, this topic is only a starting point for many other relevant developments. Encountered difficulties, coupled with suitable solutions and an assessment of reliability, as well as control approaches, are discussed in this chapter.

6.1. Difficulties and Solution Approaches

The most present difficulty is that there is no possibility for these algorithms to be tested in a real test since the new prototype is nonoperational on the point of concluding this research. In Section 5.3, a test describing the theoretical functionality is carried out. Since this was not initially resolved in the context of this thesis, the onboard verification for the contact detection remains to be done. The results are promising, yet they do not guarantee functionality in the real rover.
An other difficulty is the time delay present due to the Savitzky-Golay filter. The size of the filter for both contact detection algorithms result in a constant delay of 25 ms. This can be enhanced by increasing the internal sensory frequency and by pre-filtering the signals.

The explained video analysis that resulted in Figure 5.6 is manually made and, therefore, prone to errors. Interpolation is used to match the 60 FPS of the video to the 100 Hz of the sensory transmission, causing other inaccuracies. Therefore, the errors of Figures 5.8, 5.10 and 5.11 contain errors within themselves. This could be minimised by having 100 FPS footage or higher to analyse the contacts or external sensors, like described in Section 2.4.1.

The concept of the Calculated-Detection is based on a mathematically derived model in Chapter 3 and still has room for improvement, such as the inclusion of elastic wheel components or the extension of wheel geometries. Abstractions are chosen in the course of this thesis since the onboard computer will have to run many different programs at once, and saving computer power and computation time is to be prioritised.
This might result in an enhanced Static-Detection to be superior since this approach is simple and conserves computing power. Better tuning and pre-filtered signals could minimise errors and be suitable for contact detection in operation.
A difficulty connected to that is the phase shift, which appears when the rover is traversing steep and uneven terrain. As the calculated approach has visible phases, an earlier-than-expected contact could shift the real motor current phase, causing errors. For that, the information of the IMUs could be used in future detection, eliminating phase shifts due to underground deformations and slopes. This problem would not occur for the Static-Detection since it does not rely on the synchronisation with the motor current phase. These considerations are to be tested once the new prototype is operational.

6.2. Reliability

The result of this thesis provides two approaches to motor current-based contact detection and can therefore cover future possibilities once operation is possible. This makes access to the contact detection reliable and also adaptable.
Looking at the individual detections, errors in both detections occur to a certain degree, making room for further improvement. Which algorithm is ultimately used depends on which priority is set. If the priority is on accuracy, it can be seen that Calculated-Detection produces better results. However, if the priority is speed and simplicity, then Static-Detection is recommended.
The derived algorithms and models are easily adjustable for other rover concepts. The

number of spokes in a wheel and the dimensional parameters are pre-defined in every program and could, therefore, also be adjusted according to other use cases. Additionally the outcome of this thesis provides tools, that can post process recorded data, as long as it is saved in HDF5 files. Beyond that a video analysis tool is provided, enabling manual post processing contact detection for comparison.

6.3. Possibilities for Controllers

The availability of a contact detection has a wide spectrum of usage, mainly in controllers. When looking at walking of single-spoke rovers like the R-Hex [A+01], an increased angular velocity can be seen in periodic intervals, enabling a smoother ride, since ground contact is established faster. This approach could be transferred to the SCOUT-Rover, with the addition of coupling the contact detection to this concept. Once non-contact is detected, the wheel can increase its angular velocity and slow down again once ground contact is re-established. This is only a suggestion, but it stands to reason that this could improve the handling of the SCOUT-Rover and enhance efficiency.

Also promising is a relatively simple fault detection controller that checks the time of every contact and non-contact phase, setting a fault flag whenever this time surpasses a certain threshold. These thresholds have to scale according to the wheel's individual angular velocity. Additionally, the algorithm should verify the angular position of the wheel to see if they match the contact phase. If these additions are analysed accordingly the wheels of the rover can be prevented from jamming or spinning freely on one side. Both of these cases are, then again, a good starting point for developing further driving strategies and for robustifying the autonomous driving behaviour of the rover.

Underground mapping could also be enhanced by a contact recognition. An algorithm could map the ground contact for all wheels over time, generating contact maps. This could support the independent navigation of the rover and opens up the possibility for the rover to record environment maps completely without cameras or light.

7. Conclusion

To conclude the thesis, the initial question is to be asked:

Can a derived algorithm recognise contacts based on the motor currents for a Rimless-Wheel on the SCOUT-Rover?

This question arose from the initial considerations of the rover. In Chapter 1, the structure of the SCOUT-Rover, its specifications and mission objectives are explained. This leads to the question of whether contact estimation is even possible for the high demands of the rover.

Subsequently, it was helpful to look at the current development state of the SCOUT-Rover to see what means can be used within the platform. In addition, Chapter 2 deals with the unique features of the Rimless-Wheel concept and state of the art contact-recognising approaches. Furthermore, rover concepts that already integrate strategies for contact detection are described. Unfortunately, no rover concept was found to match SCOUT's requirements, so a new strategy had to be developed from scratch.

As part of this thesis, two Protocols (A, B) were recorded, which, on the one hand, capture important dimensional data from the rover and, on the other hand, provide driving data with associated video material. This was done to analyse motor currents and wheel-ground contacts reliably. In Chapter 3, assumptions were agreed on the basis of these recordings and a motor-wheel-model was developed. This initially purely mathematical model was tested for integrity using a simulation of the motor currents carried out in Dymola.
This led to the verification of the model and an implementation with Python. The recorded data was then analysed with a post-processing contact analysis. Additionally,

not just one but two approaches were developed for this, according to different criteria. The obtained results show only small errors, therefore confirming the initial question.

These results ultimately led to a ROS2-based algorithm described in Chapter 4. This is developed for a future prototype and delivers promising results for simulated operation. Furthermore, these results can be applied to every motor and wheel, since a ROS2-messaging convention was written. This creates the framework for making all sensor data available to the future system.
All these results are summarised and explained in Chapter 5, with a particular focus on the differences between the two detection approaches.
The last contribution of this thesis is the Chapter 6 with an outlook on further topics that can be dealt with in the context of contact recognition.

In conclusion, the developed algorithm demonstrates promising potential for recognising contacts based on motor currents for the Rimless-Wheels on the SCOUT-Rover. This addresses the initial question and provides additional insights for future advances in contact detection technology for terrestrial and extraterrestrial rover applications.

8. Bibliography

[A+01] R. Altendorfer et al. Rhex: A biologically inspired hexapod runner. *Autonomous Robots*, 11:207–213, 2001.

[ADMa16] Sharda Prasad Agrawal, Haresh Dagale, Nirmal Mohan, and et. al. IONS: A Quadruped Robot for Multi-terrain Applications. *International Journal of Materials, Mechanics and Manufacturing*, 4(1):84–88, 2016.

[Ari10] Thawar T. Arif, editor. *Aerospace Technologies Advancements*. INTECH Open Access Publisher, Vukovar, Croatia, 2010.

[Asu23] AAEON Asus. Pico-kbu4, 2023. `https://www.aaeon.com/en/p/pico-itx-boards-pico-kbu4?dl=datasheet` [Accessed: 22.02.2024].

[Ave20] André Avez. *Differential calculus*. Courier Dover Publications, 2020.

[B+22] Stefan Barthelmes et al. MMX Rover Locomotion System – Development and Testing towards the Flight Model. In *Proceedings of the 2022 IEEE Aerospace Conference, 5-12 March 2022, Big Sky, MT, USA*. IEEE, 2022.

[Bar20] Stefan Barthelmes. *Model-based chassis control of a wheeled mobile robot on soft ground using the example of the ExoMars Planetary Exploration Rover*. Dissertation, Technische Universität Darmstadt, Darmstadt, Germany, 2020.

[BPB23] Fabian Buse, Antoine Francois Xavier Pignede, and Stefan Barthelmes. A modelica library to add contact dynamics and terramechanics to multi-body mechanics. In *Proceedings of the 15th International Modelica Conference*,

volume 204 of *Linköping Electronic Conference Proceedings*. Modelica Association, Oktober 2023.

[CLKa17] Haedo Cho, Hyosang Lee, Yeongjin Kim, and et. al. Design of an optical soft sensor for measuring fingertip force and contact recognition. *International Journal of Control, Automation and Systems*, 15(1):16–24, Feb 2017.

[FBSMa15] Wolfgang Fink, Victor R. Baker, Dirk Schulze-Makuch, and et. al. Autonomous exploration of planetary lava tubes using a multi-rover framework. In *2015 IEEE Aerospace Conference*, pages 1–9, 2015.

[FPAa20] Peter Fritzson, Adrian Pop, Karim Abdelhak, and et. al. The OpenModelica Integrated Environment for Modeling, Simulation, and Model-Based Development. *Modeling, Identification and Control*, 41(4):241–285, 2020.

[GZZa23] Weiwei Geng, Ting Zhu, Yuqing Zhang, and et. al. Rotor air-friction loss and thermal analysis of ipm rotors for high speed axial-flux machine. *IEEE Transactions on Industry Applications*, 59(1):779–788, 2023.

[HBB17] Matthias Hellerer, Stefan Barthelmes, and Fabian Buse. The dlr rover simulation toolkit. In Eveline van Beekhuizen, editor, *14th symposium on advanced space technologies in robotics and automation*. ESA's Automation and Robotics group, Juni 2017.

[Kiu13] Jaan Kiusalaas. *Numerical methods in engineering with Python 3*. Cambridge university press, 2013.

[Koc23] Johannes Koch. Integration and analysis of a slam platform for the dlr scout rover using two compliantly-connected rgb-d cameras. Master's thesis, School of Engineering and Design Aerospace and Geodsy, 2023.

[KS12] Sunder Ram Krishnan and Chandra Sekhar Seelamantula. On the selection of optimum savitzky-golay filters. *IEEE transactions on signal processing*, 61(2):380–391, 2012.

[Lan23] Michael Lange. *Chassis und Separationsmechanismus des IDEFIX-Rovers*. PhD thesis, DLR, 2023.

[LD10] Richard J. Léveillé and Saugata Datta. Lava tubes and basaltic caves as astrobiological targets on earth and mars: A review. *Planetary and Space Science*, 58(4):592–598, 2010.

[LSFa23] Roy Lichtenheldt, Manuel Schütt, Dennis Franke, and et. al. Towards robotic exploration of extraterrestrial caves - the first in-cave tests of the DLR Scout rover. In *Proceedings of the 4th International Planetary Caves Conference, 4-7 May 2023, Lanzarote, Spain*. LPI, 2023.

[Max21a] Maxon. Encoder 16 easy 128–1024 cpt, 3 channels, with line driver rs 422, 2021. `https://www.maxongroup.de/maxon/view/category/motor?etcc_cu=onsite&etcc_med_onsite=Product&etcc_cmp_onsite=RE+Programm&etcc_plc=Overview-Page-DC-Motors&etcc_var=%5bde%5d%23de%23_d_&target=filter&filterCategory=re` [Accessed: 08.02.2024].

[Max21b] Maxon. Planetary gearhead gp 42 c, 2021. `https://www.maxongroup.de/maxon/view/category/motor?etcc_cu=onsite&etcc_med_onsite=Product&etcc_cmp_onsite=RE+Programm&etcc_plc=Overview-Page-DC-Motors&etcc_var=%5bde%5d%23de%23_d_&target=filter&filterCategory=re` [Accessed: 08.02.2024].

[Max22] Maxon. Re 40, 40 mm, graphite brushes, 150 watt, 2022. `https://www.maxongroup.de/maxon/view/category/motor?etcc_cu=onsite&etcc_med_onsite=Product&etcc_cmp_onsite=RE+Programm&etcc_plc=Overview-Page-DC-Motors&etcc_var=%5bde%5d%23de%23_d_&target=filter&filterCategory=re` [Accessed: 08.02.2024].

[McG90] Tad McGeer. Passive dynamic walking. *The International Journal of Robotics Research*, 9(2):62–82, 1990.

[Mil15] Dubravko Miljković. Brief review of motor current signature analysis. *HDKBR Info magazin*, 5(1):14–26, 2015.

[MKA16] Yuya Maruyama, Shinpei Kato, and Takuya Azumi. Exploring the performance of ros2. In *Proceedings of the 13th International Conference on Embedded Software*, pages 1–10, 2016.

[MKLa11] Jörg Mämpel, Sebastian Köhring, Roy Lichtenheldt, and et. al. ROLV – A Hybrid Wheel Robot Using Compliant Mechanisms for Locomotion. In *Proceedings of the 5th International Symposium on Adaptive Motion of Animals and Machines (AMAM), 11-14 October 2011, Hyogo, Japan*, pages 23–24, 2011.

[OV98] S.J. Ovaska and S. Valiviita. Angular acceleration measurement: a review. In *IEEE Instrumentation and Measurement Technology Conference. Where Instrumentation is Going*, volume 2, pages 875–880 vol.2, 1998.

[PAAa16] FITA Petrescu, Antonio Apicella, Raffaella Aversa, and et. al. Something about the mechanical moment of inertia. *American Journal of Applied Sciences*, 13(11):1085–1090, 2016.

[PL22] Antoine Pignède and Roy Lichtenheldt. Modeling, simulation and optimization of the DLR Scout rover to enable extraterrestrial cave exploration. In *Proceedings of the 6th Joint International Conference on Multibody System Dynamics (IMSD) and the 10th Asian Conference on Multibody Dynamics (ACMD), 16-20 October 2022, New Delhi, India*. Springer, 2022.

[PLKa12] Changhyun Pang, Gil-Yong Lee, Tae-il Kim, and et. al. A flexible and highly sensitive strain-gauge sensor using reversible interlocking of nanofibres. *Nature Materials*, 11(9):795–801, Sep 2012.

[PSFa23] Antoine Pignède, Manuel Schütt, Dennis Franke, and et. al. The DLR Scout Rover During The 2022 ARCHES Demomission Space On Mount Etna: Operating The Rover Outside Of Its Comfort Zone. In Andreas Strohmayer and Roland Gerhards, editors, *Proceedings: 72. Deutscher Luft- und Raumfahrtkongress 2023 (DLRK), 19-21 September 2023, Stuttgart, Germany*. DGLR, 2023.

[PSLa22] Antoine Pignède, Walter Schindler, Roy Lichtenheldt, and et. al. Toolchain for a Mobile Robot Applied on the DLR Scout Rover. In *Proceedings of the 2022 IEEE Aerospace Conference, 5-12 March 2022, Big Sky, MT, USA*. IEEE, 2022.

[PSO02] Christopher Pelchen, Christian Schweiger, and Martin Otter. Modeling and simulating the efficiency of gearboxes and of planetary gearboxes. In *Proceedings of 2nd International Modelica Conference*, pages 257–266, März 2002.

[SA94] H. Shinoda and S. Ando. Ultrasonic emission tactile sensor for contact localization and characterization. In *Proceedings of the 1994 IEEE International Conference on Robotics and Automation*, pages 2536–2543 vol.3, 1994.

[SAK15] Roland U. Sonsalla, Joel Bessekon Akpo, and Frank Kirchner. Coyote III: Development of a Modular and Highly Mobile Micro Rover. In *Proceedings of the 13th Symposium on Advanced Space Technologies in Robotics and Automation (ASTRA), 10-13 May 2015, Noordwijk, The Netherlands*. ESA, 2015.

[SBB21] Juliane Skibbe, Stefan Barthelmes, and Fabian Buse. Locomotion control functions for the active chassis of the mmx rover. In *2021 IEEE Aerospace Conference (50100)*, pages 1–9. IEEE, 2021.

[Ski21] Juliane Skibbe. Analysis of Phase Shifts for a Rimless Wheel Rover. In *Proceedings of the 2021 IEEE Aerospace Conference, 6-13 March 2021*. IEEE, 2021.

[SLBa17a] Leon Stubbig, Roy Lichtenheldt, Felix Becker, and et. al. Model-based development of a compliant locomotion system for a small scout rover. Technical report, TU Ilmenau, 2017. `https://nbn-resolving.org/urn:nbn:de:gbv:ilm1-2017iwk-012:0` [Accessed: 09.11.2023].

[SLBa17b] Leon Stubbig, Roy Lichtenheldt, Felix Becker, and et. al. Model-based development of a compliant locomotion system for a small scout rover. In

Proceedings of the 59th Ilmenau Scientific Colloquium, 11–15 September 2017, Ilmenau, Germany. Universitätsverlag Ilmenau, 2017.

[UMGa21] Stephan Ulamec, Patrick Michel, Matthias Grott, and et. al. Scientific Objectives of the MMX Rover Mission to Phobos. In *Proceedings of the Global Space Exploration Conference (GLEX 2021), 14-18 June 2021, St Petersburg, Russia*. IAF, 2021.

[VRD09] Guido Van Rossum and Fred L Drake. Python, 2009.

Appendix

A. Protocol: Motor Current Testcases on the DLR SCOUT-Rover

Justus Jentsch
22.01.2024 - 23.01.2024
Planetary Exploration Lab, Room K317, Building 135, DLR-Oberpfaffenhofen

Test Description

The aim of this test is to analyse the motor currents of the SCOUT-Rover and make them accessible through camera recordings. To achieve this, different test cases are recorded three times each with varying duration and then compared. The corresponding video recordings aim to clarify the relationship between the motor current and the actual processes. The test case conditions remain constant, with only the running time increasing for each test case.

A total of five test cases are to be conducted in this protocol, resulting in 15 recordings that are compared. The first two cases aim to verify the estimated motor currents and establish upper and lower boundaries for the motor currents that occur. The third and fourth tests provide information on potential variations in motor currents across different gaits. Theoretically, in tripod driving mode, there are instances where a wheel does not make contact with the ground, which should be identifiable in the motor current graph. The final case should appear random, thereby confirming non repetitive patterns.
The primary objective is to identify significant distinctions between case 1 and case 2, and within the other test cases.

Case Description

1. Wheels of the SCOUT-Rover spin freely.

2. Wheels 01 and 06 of the SCOUT-Rover do not spin, but the motors are powered. Achieved by fixating the Rover on a test bench.

3. SCOUT-Rover drives on flat and horizontal ground with constant speed in a straight line with synchronous wheel mode.

4. SCOUT-Rover drives on flat and horizontal ground with constant speed in a straight line with tripod wheel mode.

5. SCOUT-Rover drives over test site in tripod mode, without instructions or restrictions.

Material List:

1. Stopwatch (Smartphone)

2. SCOUT-Rover

3. Gamepad

4. Camera

5. Test Bench

6. SCOUT Operating Computer

7. SCOUT Communication Antenna

Evaluation

Table A.1 displays the cases, time stamp, recording duration, associated file name, and resulting functional graph. A Python script is used to extract the Time and Motor 01 current data, which are then plotted in relation to each other.

For case 1, it is evident that initiating the motor causes a spike in current. Subsequently, the current stabilises. The results indicate minimal deviation. Similarly, releasing the motor also causes a spike. In standby mode, the motor does not consume power, resulting in negligible current compared to the powered state. The current oscillates around an -40 mA offset with an amplitude of 45 mA.
For case 2, the SCOUT was not driven on the ground but was instead mounted on a test rig. Two diagonal motors are fixed to the floor of the test rig using a durable string, while the chassis of the SCOUT was secured with clamps. The SCOUT body remained in the same position throughout the test. The impulse on the Gamepad used to control the SCOUT was given when loaded. The results also appeared as expected, with current spikes occurring during initialisation. The Elmo Motion Controller's over current protection (OCP) activates and shuts power supply down, resulting in a brief but high spike of up to 400 mA. It is likely that the sampling rate of 100 Hz is too low to see the full magnitude of the current. Based on other tests and the limit for the over current protection, the current had to be at least 3 A.
The third case involves driving the rover on flat ground in a straight line using synchronous wheel mode. This results in an oscillating behaviour that is clearly visible when a foot hits the ground and lifts the chassis. The ascent is steep at the point of contact and then flattens out. This is expected as a significant amount of force is required initially to raise the rover. However, after reaching its highest point, it requires no energy to lower it. The spikes range from 400 mA to -400 mA.
Case 4 was tested under the same conditions, except for the tripod gait. The overall current spikes are much smaller, ranging only around 200 mA to -200 mA. However, due to only 3 legs lifting the entire mass of the rover during initialisation, a higher spike resulted. In this test, it even reached almost 1 A.
The final case aims to verify that random inputs result in random motor current outputs. An intern conducted three tests by driving the rover on the Planetary Exploration Lab test field (PEL) without any specific instructions. The plot shows no regularity.

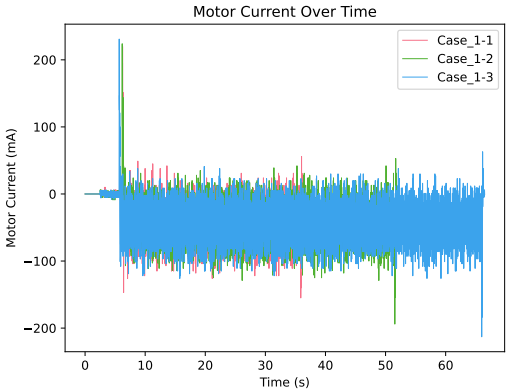

(a) Time course of first case.

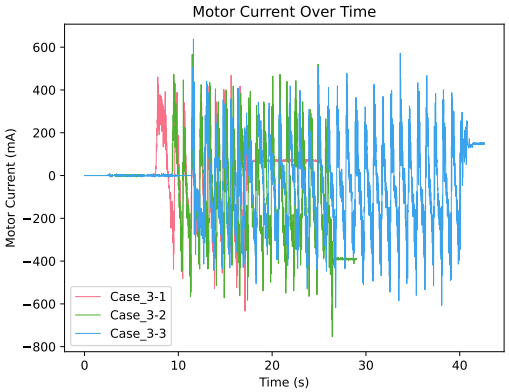

(b) Time course of third case.

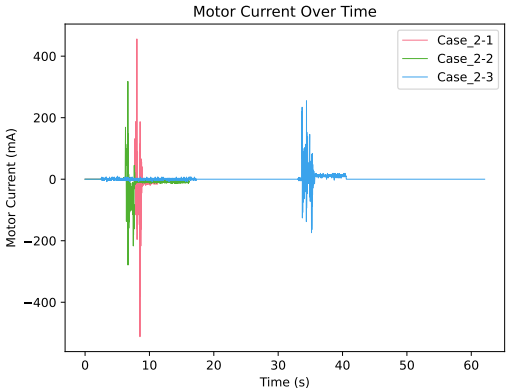

(c) Time course of second case.

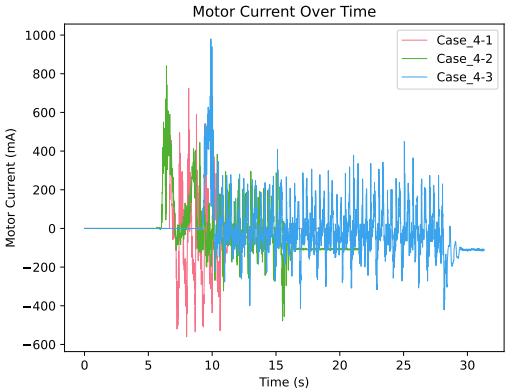

(d) Time course of fourth case.

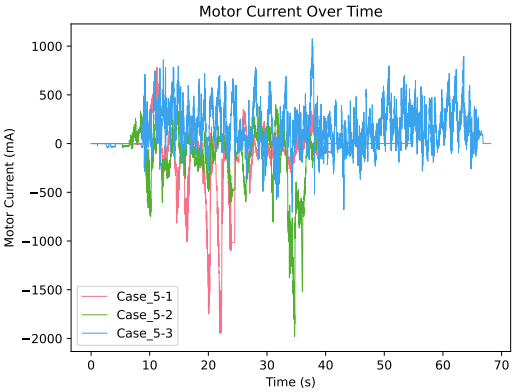

(e) Time course of fifth case.

Table A.1.: Measurement Protocol for SCOUT-Rover test cases.

Case	Attempt	Time	Duration	Associated Files
1	1	10:48	31 sec	ScoutHardwareOut_1-1.h5
	2	10:51	46 sec	ScoutHardwareOut_1-2.h5
	3	10:53	62 sec	ScoutHardwareOut_1-3.h5
2	1	14:58	03 sec	ScoutHardwareOut_2-1.h5
	2	15:00	03 sec	ScoutHardwareOut_2-2.h5
	3	15:05	05 sec	ScoutHardwareOut_2-3.h5
3	1	08:25	12 sec	ScoutHardwareOut_3-1.h5
	2	08:27	21 sec	ScoutHardwareOut_3-2.h5
	3	08:29	31 sec	ScoutHardwareOut_3-3.h5
4	1	08:34	11 sec	ScoutHardwareOut_4-1.h5
	2	08:43	21 sec	ScoutHardwareOut_4-2.h5
	3	08:47	25 sec	ScoutHardwareOut_4-3.h5
5	1	11:02	31 sec	ScoutHardwareOut_5-1.h5
	2	11:05	45 sec	ScoutHardwareOut_5-2.h5
	3	11:25	65 sec	ScoutHardwareOut_5-3.h5

(a) Setup for case one with all wheels lifted from the ground.

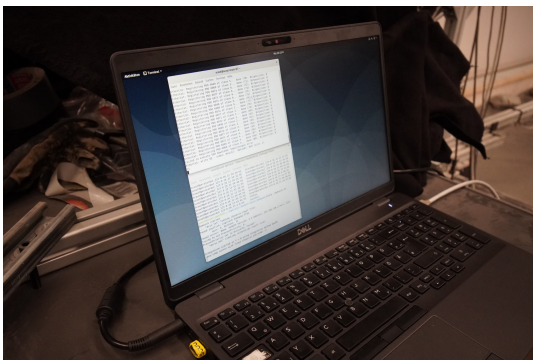

(b) SCOUT operating computer initialising launch command.

Figure A.2.: First test setup.

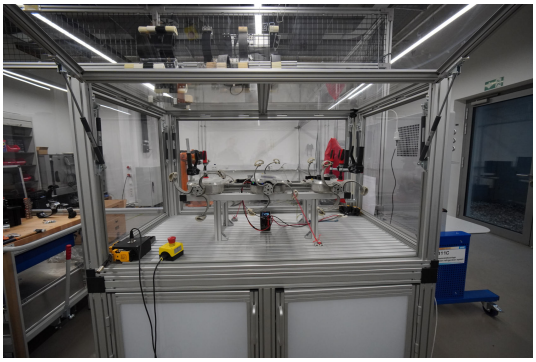

(a) Test bench used for case two.

(b) Close up view on wheel fixation.

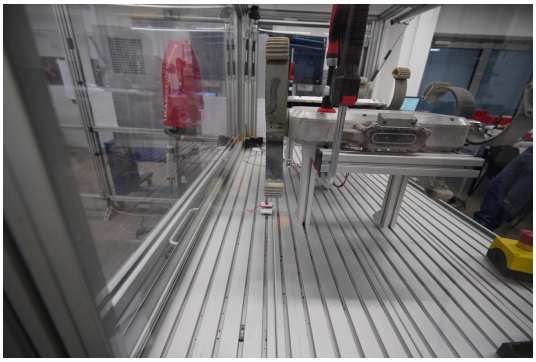

(c) Front view of the test bench and fixed SCOUT.

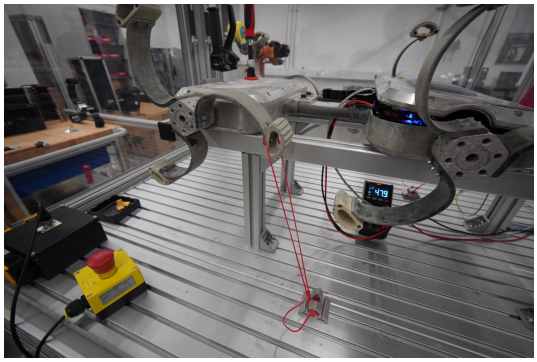

(d) Rimless wheel under initialisation tension.

Figure A.3.: Test bench setup for case two.

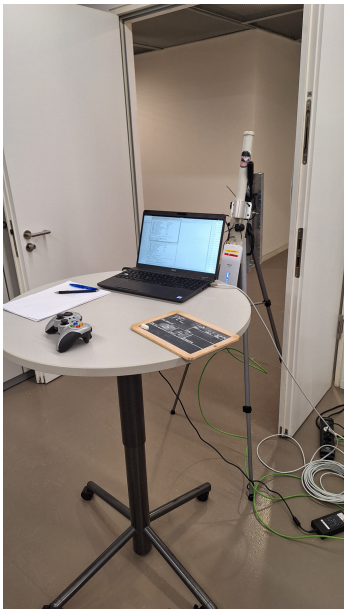

(a) Setup for cases three and four.

(b) Straight path in front of PEL.

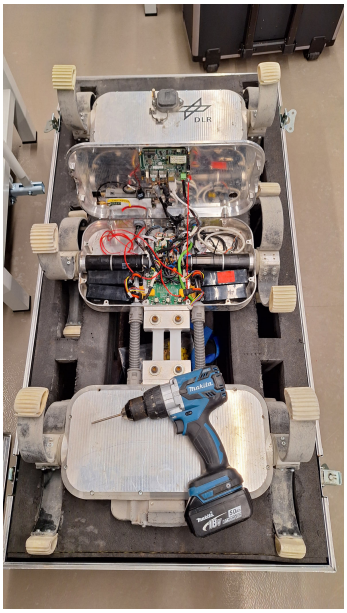

(c) SCOUT assembly for testing.

Figure A.4.: Test setup for cases three and four.

(a) SCOUT following commands for case 5.

(b) Surface of the Planetary Exploration Lab test field.

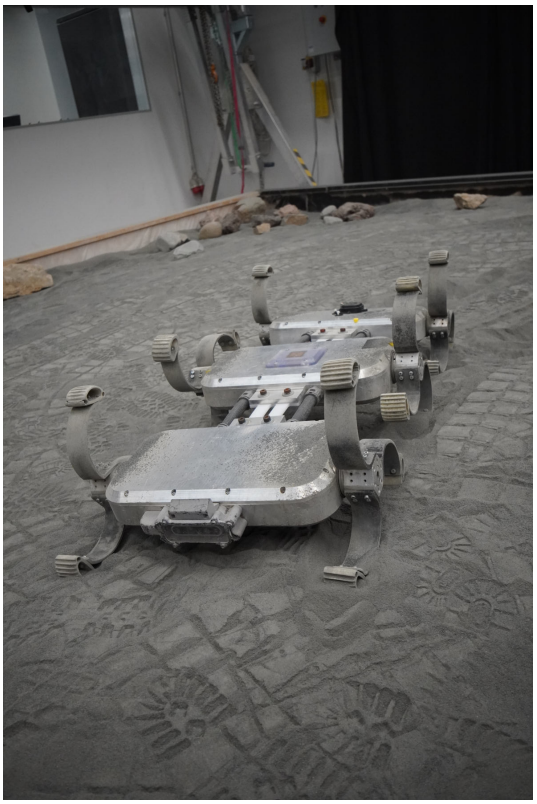

(c) SCOUT is preparing for next test.

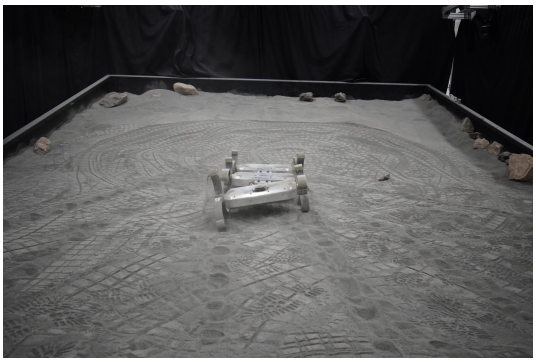

(d) SCOUT climbing an incline.

Figure A.5.: Planetary Exploration Lab tests.

B. Protocol: Weight Measurements on SCOUT-Rover Parts

Justus Jentsch
09.01.2024 and 26.01.2024
Vaporcycle and Industry Robotics Lab, Room K407 and CNC Machining hall, Room 0411, Building 135, DLR-Oberpfaffenhofen

Test Description

The objective of this test is to analyse the weight of the SCOUT-Rover as a whole, the weight distribution on its individual wheels, and to estimate the weight of its wheel components. To achieve this, three measurements are taken and averaged. Technical term abbreviations are explained upon first use. Each measurement follows the same procedure: levelling the scales, placing the object on the scales, and recording the weight once it stabilised.

Measurements

1. Weight of wheel mounting
2. Weight of spoke
3. Weight of foot
4. Weight of whole wheel
5. Weight of whole SCOUT
6. Weight on motor 01
7. Weight on motor 04
8. Weight on motor 06

Material List:

1. Weight scale PM34 DeltaRange
2. Weight scale Kern CFS
3. Camera
4. SCOUT-Rover
5. Rimless wheel spoke
6. Rimless wheel foot
7. Rimless wheel foot
8. Rimless wheel

Evaluation

The results of the measurements can be seen in Table B.1. Both scales can display one kilogram to the fourth decimal. The measured values shown are not rounded and have an error tolerance of 0.1%. Cases 1 - 4 seem to be very precise, since the values are very close together. Proven by the summation of all parts, which approximately matches with the total mass of the wheel in case four.

$$m_M + 3 \cdot m_S + 3 \cdot m_F = m_{W_{sum}} = 531.4 \text{ g} \tag{B.1}$$

$$m_{W_{sum}} - m_{W_{real}} = -58.15 \text{ g} \tag{B.2}$$

Combining all the parts results in 58.15 g difference in weight. This is due to the missing screws, nuts and washers. Looking at the difference between the sum of case 6 to 8 and case 5 is more drastic.
Note that it is assumed that the rover is symmetrical in its composition along its longitudinal section. Therefore a measurement of motors 02, 03 and 05 is not necessary since they should produce approximately the same weight. Obviously this is a source of error, but to keep the simplicity it is assumed that the pairings weigh the same. ($m_{01} = m_{02}$, $m_{03} = m_{04}$, $m_{05} = m_{06}$)

Table B.1.: Measurement Protocol for SCOUT-Rover weight.

Case	Attempt	Weight	Mean Value
1	1	247.6 g	
	2	247.6 g	247.6 g
	3	247.6 g	
2	1	67.6 g	
	2	67.5 g	67.6 g
	3	67.4 g	
3	1	26.9 g	
	2	27.1 g	27 g
	3	27 g	
4	1	589.4 g	
	2	589.6 g	589.55 g
	3	589.3 g	
5	1	20.001 kg	
	2	20.001 kg	20.001 kg
	3	20.001 kg	
6	1	3.073 kg	
	2	2.981 kg	3.017 kg
	3	2.996 kg	
7	1	4.937 kg	
	2	5.088 kg	5.016 kg
	3	5.022 kg	
8	1	2.974 kg	
	2	2.917 kg	2.929 kg
	3	2.896 kg	

$$2 \cdot m_{01} + 2 \cdot m_{04} + 2 \cdot m_{06} = m_{sum} = 21.924 \text{ kg} \tag{B.3}$$

$$m_{sum} - m_{real} = 1.923 \text{ kg} \tag{B.4}$$

This result is more different than expected and therefore an error in the measurement setup can be surmised. Never the less a correcting quotient can be calculated:

$$Q_1 = \frac{m_{sum}}{m_{01}} = 7.2668$$

$$Q_2 = \frac{m_{sum}}{m_{04}} = 4.3708 \tag{B.5}$$

$$Q_3 = \frac{m_{sum}}{m_{06}} = 7.4851$$

With these ratios the new relative masses lasting on front, middle and rear motors can be calculated:

$$m_f = \frac{m_{real}}{Q_1} = 2.7522 \text{ kg}$$

$$m_m = \frac{m_{real}}{Q_2} = 4.5758 \text{ kg} \tag{B.6}$$

$$m_r = \frac{m_{real}}{Q_3} = 2.6719 \text{ kg}$$

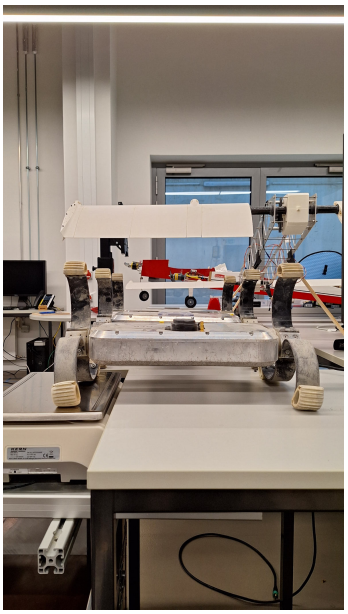

(a) Front view of measuring setup for case 8.

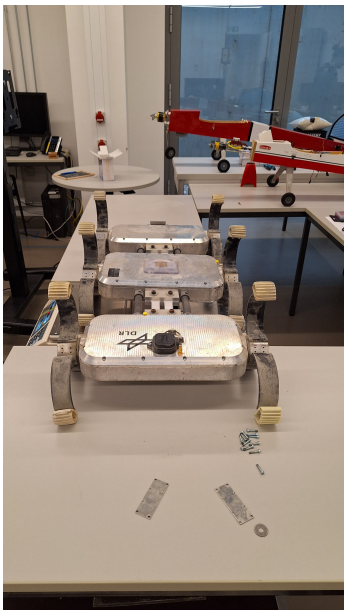

(b) Front view of measuring setup for case 7.

(c) Verification that scale is orthogonal to the floor.

(d) Side view of measuring setup for case 7.

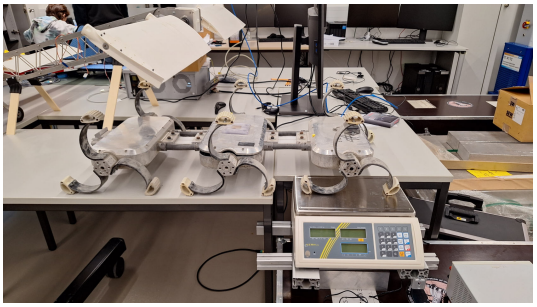

(e) Side view of measuring setup for case 6.